Title:

Motile Living Biobots Self-Construct from Adult Human Somatic Progenitor Seed Cells

Gizem Gumuskaya[1 2], Pranjal Srivastava[1]*, Ben G. Cooper[1]*, Hannah Lesser[1], Ben Semegran[1], Simon Garnier[3], and Michael Levin[1 2**]

[1] Allen Discovery Center at Tufts University, and Department of Biology, Tufts University, Medford, MA, USA
[2] Wyss Institute for Biologically Inspired Engineering, Harvard University, Boston, MA 02115
[3] Federated Department of Biological Sciences, New Jersey Institute of Technology, Newark, NJ 07102, USA.

* These authors contributed equally.

** Corresponding Author:
Dr. Michael Levin
Allen Discovery Center at Tufts University,
Tufts University
200 Boston Avenue, suite 4600
Medford, MA 02155-4243
Phone: +1 617 627 6161
Email: michael.levin@tufts.edu

Keyword: biobot, bioengineering, morphogenesis, self-assembly, emergence

Running title: Adult human cell-based biobots

Email: Gizem.gumuskaya@tufts.edu

Abstract

Fundamental knowledge gaps exist with respect to the plasticity of cells from adult soma and the potential diversity of body shape and behavior in living constructs derived from such genetically wild-type cells. Here we introduce Anthrobots, a spheroid-shaped multicellular biological robot platform with diameters ranging from 30 to 500 microns. Anthrobots have an inherent capacity for motility in aqueous environments, via cilia covering their surface. Each Anthrobot starts out as a single cell, derived from the adult human lung, and self-construct into a multicellular motile biological machine after having been cultured in extra cellular matrix for 2 weeks, followed by a transfer into a minimally viscous and adhesive habitat. Anthrobots exhibit a wide range of behaviors with motility patterns ranging from tight loops to straight lines with speeds ranging from 5-50 microns/second. Our anatomical investigations reveal that this diversity in their movement types is significantly correlated with their diversity in morphological types. Anthrobots can assume diverse morphologies from fully polarized to wholly ciliated bodies with spherical or ellipsoidal shapes, each correlating with a distinct movement type. Anthrobots were found to be able to traverse live human tissues in various ways as a function of these different movement types. Remarkably, Anthrobots are shown to be able to induce rapid repair of wounds in human neural cell sheets in vitro. By controlling microenvironmental cues, entirely novel structure, behavior, and biomedically-relevant capabilities can be discovered in morphogenetic processes not requiring direct genetic manipulation.

Highlights:

- This work is part of the existing science of organoids and synthetic bioengineering
- Anthrobots are made from discarded tracheal epithelial (skin) cells of adult patients
- The cells self-organize, in a dish, into tiny clusters of cells that swim around by waving cilia (which other animals use, and the human trachea uses to propel particles out of the airway)
- They are related to Xenobots, showing that the Xenobot phenomenon is not due to special features of embryonic or of amphibian cells – adult human cells do it too, which suggests this is a wide-spread cellular capability
- No transgenes were used – their abilities are completely natural
- Biobots are a platform for learning about native cellular intelligence, and showing how life explores new ways of being (cellular creativity, competency, plasticity)
- Anthrobots can heal wounds in neural tissue; it is not known yet what other surprising behaviors and capabilities they may have
- Potential future positive impacts and uses – bio-robotics for regenerative medicine:
    - Chasing down cancer cells in your gut
    - Putting down pro-regenerative drugs or other molecules
    - Out of the body sculpting engineered tissue for transplantation
    - Patient-specific avatars for drug testing = personalized medicine (reduces animal testing use, while showing you effects of drugs on your own tissues)
- Safety aspects
    - Made of patient's own cells - no problem with immune rejection and no need for immune suppressing medication
    - Limited life span – they only live a few weeks
    - Biodegradable
    - Very stringent survival requirements – they can't live outside of a very specific lab culture environment (unlike all the artificial bacteria and viruses made today)
    - They do not reproduce
    - Not genetically-modified
- Ethics
    - No embryonic cells used, so no human (and no animal) was negatively impacted
    - Skin only, so concern for their welfare should be much less than for brainy experimental or food animals like fish or cows
    - We view this as a new tool with which to advance the moral responsibility to actively reduce human and animal suffering from biomedical causes

Introduction

Fundamental questions in evolutionary, developmental, cell, and synthetic biology revolve around the issue of morphogenetic plasticity: the range of anatomical and behavioral phenotypes that emerge from cells with a specific genome. Exploring the rules of multicellular self-assembly toward adaptive function is critical for understanding the evolution of body-plans, and for developing interventions in regenerative medicine which coax cells toward rebuilding desired complex structures[1]. By confronting cells with new microenvironments and signals, and focusing on the emergent (spontaneous) self-assembly and resulting functionality in physiological, transcriptional, and physical spaces[2,3], much can be learned about the mesoscale rules governing collective cell behavior and the relative contributions of genetic and generic laws of form[4–8].

Another key field impacted by this question is bioengineering and synthetic biology, more specifically synthetic morphogenesis – the development of self-constructing living structures by design with predictable and programmable properties[9–26]. Biobots is a related, rapidly growing field, focusing on building new kinds of living machines[27–31]. In the last decade, interest in developing biobots, which often come in the form of motile biogenic assemblies, have seen a rapid surge [32,33]. Early examples of biobots are hybrids between biological cells and inert chemical substances supporting them, such as gels or 3D-printed scaffolds [34–38]. These efforts were recently followed by Xenobots, fully-cellular biobots created from frog epithelial cells that are motile and do not require external pacing[39–41].

Xenobots exhibit a range of surprising behaviors and capabilities, hinting at the plasticity of cellular self-assembly toward novel structures and functions, and raised a number of key open questions. First, could adult, somatic cells exhibit the same kind of surprising capability, or is this level of morphological and functional plasticity limited to embryonic material? Second, was their novel phenotype due to their origin in amphibians – known for morphological plasticity? If human cells had such capacities, this would have implications for understanding the modifications to cell behavior that implement multicellularity, as well as open opportunities for patient-relevant living machines in biomedical contexts. Third, could a biobot be made of mammalian cells without exogenous synthetic biology circuits or genomic editing – do wild-type mammalian cells have capacities to build novel functional architectures from the exact same genome? If so, what surprising capabilities might be revealed? And finally, could a high-throughput process be developed that produces large numbers of biobots in parallel without the manual extraction, or use of animals, needed to acquire material, as was the case for Xenobots?

Here, we introduce new biodegradable, fully organic, motile living constructs created out of human lung epithelium. We refer to them as Anthrobots, in light of their human origin and potential as a biorobotics platform[27,30,31,42], and quantify their emergent, baseline properties as an essential background characterization of their native capacities from which future efforts to reprogram form and function will flow. Anthrobots self-assemble in vitro, via a fully scalable method that requires no external form-giving machinery, manual sculpting, or embryonic tissues and produces swarms of biobots in parallel. They move via cilia-driven propulsion, living for 45-60 days. We quantitatively characterized the range of movement and morphotypes, showing that their behaviors are strongly correlated with specific features of their anatomy. The ability of adult, somatic, human cells to form a novel functional anatomy, with unique behaviors, reveals that this plasticity is not restricted to amphibian or embryonic cell properties, and is a fundamental feature of wild-type cells that requires no direct genetic manipulation to unlock. Apical-out lung organoids created using various methods have very recently been reported[43,44]; however, no significant translocation has been shown. Remarkably, Anthrobots exhibit a behavior completely unexpected

given their origin as static tracheal epithelium: they can traverse wounds in (human) neural tissue and induce repair. Numerous in vitro and in vivo uses of such living machines can be envisioned, especially because they can now be made of the patient's own cells. Thus, we show that the human genome encodes cellular hardware with morphogenetic, behavioral, and functional potential that goes far beyond the familiar default outcomes in vivo, potentially enabling a range of biomedical applications in addition to hinting at new aspects of evolutionary developmental biology.

Results

Human bronchial epithelial cells self-construct into multicellular motile living architectures.

Is the ability to make a self-propelled, multicellular living construct, with a body structure and behavior different from the species-default, despite its wild-type genome, limited to embryonic amphibian tissues? Hypothesizing that anatomical and behavioral plasticity was a fundamental property of cell collectives, we chose a cell source that might be least expected to reveal novel morphogenetic activity: adult, human, somatic, progenitor cells from elderly patients. In order to explore and exploit morphogenetic plasticity of adult human cells, we hypothesized that novel multicellular constructs with autonomous locomotion could be created via progenitor cells' innate developmental capacity. To study and steer the in vitro morphogenesis of novel three dimensional tissues with motile appendages, we developed a novel protocol (Figure 1A) that builds upon the existing ability of human bronchial epithelium progenitor cells to form monoclonal spheroids (Figure 1-a.1) with cilia-lined lumina[45–48] (i.e., apical-in configuration). We modified this process by manipulating the culture environment such that it now yields cilia-coated (i.e., apical-out configuration) self-constructing spheroids, which exhibit spontaneous locomotive ability.

A key step in their construction, in order to obtain significant translocation, is inducing the cilia to face outward. Given that cilia naturally localize into the lumen due to the basal cells' interaction with the surrounding high-viscosity matrix, we hypothesized that changing the culture environment to a lower viscosity level (e.g., water-based media instead of gel-based matrix) may trigger the basal layer cells to migrate inward and allow the apical layer to take their place on the spheroid cortex[49]. Thus, in order to trigger apicobasal polarity switching, we first grew airway organoids embedded in Matrigel as has been done previously[50] (Figure 1-a.2), and then we dissolved the surrounding matrix and transferred the spheroids into a low-adhesive dish (Figure 1-a.3). We observed that in this new low viscosity environment, originally apical-in spheroids that show no motility on day 0 (Figure 1-b.1) became motile by day 7 (Figure 1-b.2).

To characterize the temporal dynamics of motility initiation, we periodically (bidaily) counted the number of spheroids that became motile for 3 weeks following dissolution and observed a sigmoidal motility profile with peak change in motility on day 10 (Figure 1C). We next confirmed that this drastic change in motility occurred as a result of a morphological reorganization event exposing cilia on the cortex (Figure 1D). We immunostained the spheroids on day 0 (pre-motility) and day 7 (post-motility) with DAPI and for the apical markers a-tubulin (cilia marker) and ZO1 (tight junction marker), revealing a drastic increase in multi-ciliated cells on day 7 compared to day 0. Figure 1E shows the tissue organization within an approximately 50-micron depth of a typical Anthrobot (darker colors representing the deeper layers).

Anthrobots self-organize into discrete movement types.

Despite their wild-type human genome and somatic basis, these cells produce discrete, self-motile constructs with a wide range of behaviors and an anatomy that differs from the species-specific morphology expected from their human tissue origin. As with any new organism[2], a key task is to determine whether its major behaviors are discrete characters or continuous ones[51,52]. Thus, we quantitatively analyzed their range of behavior modes in timelapse videos of approximately 200 randomly-selected motile spheroids (Figure 2A, see supplemental videos 1-4) for 5 hours in groups of 4 or 5 Anthrobots, and extracted their movement trajectory coordinates. We then split up these 5 hour-long trajectories into 30 second periods to classify behavior with a higher degree of granularity and in an aggregate manner. To identify patterns within a potentially unlimited set of possible movements, we characterized these trajectories by how straight and/or circular they are as all possible trajectories can be explained together by these two properties. To this end, we developed two main trajectory characterization metrics: straightness and gyration indices (see Methods for detailed description of how these indices are calculated) and plotted all viable trajectorial periods along these two indices (Figure 2B). We then ran an unsupervised clustering algorithm on this landscape, which revealed four statistically distinct clusters (Figure 2C). Further investigation of these clustering sub-populations suggested each represents a distinct movement type: circular, linear, curvilinear and eclectic (Figure 2D). Figure 2E shows the homogeneity and size characterization of each cluster and Figure 2F shows a quantitative comparison of different clusters along the two major movement indices.

Circular bots (type 1, Figure 2D) score the highest on gyration and lowest on straightness indices (Figure 2F). They also have the smallest dissimilarity index and contains over 30% of all the periods (Figure 2E), meaning they have highly similar trajectories in terms of shape and are very common among the behaviors of spheroids as a whole. Linear bots (type2, Figure 2D) score the highest on straightness and lowest on gyration indices (Figure 2F). They have a higher dissimilarity than circular bots but also have the greatest number of periods out of all clusters (Figure 2E). Circular and linear bots together make up more than half of the population, and each have the most homogeneous populations among all movement types. Finally, the third most common (Figure 2E) type of bot is the curvilinear bot (type 3, Figure 2D), which scores high on both the gyration and straightness indices (Figure 2F) and has the second most heterogeneous trajectories (Figure 2E). Bots with most disorganized trajectories and smallest representation in the overall population (Figure 2E) are the eclectic bots (type 4, Figure 2D), which score the lowest on both the gyration and straightness indices (Figure 2F) due to exhibiting eccentric trajectories that are often a combination of the other three types.

We continued the characterization of this novel system's behavior by testing the sequences of its various discrete behaviors and their transition probabilities [53–55] : is there a pattern describing how the individual behaviors extracted from trajectory domains follow each other during a bot's lifetime? In order to investigate the stability of each trajectory, we used a Markov chain to concatenate the successive periods of a given trajectory and thus reconstruct each bot's path. Figure 2G features the Markov chain of all ~200 bots we included in this movement type characterization analysis and shows the circular bots (type 1) as the most committed category with 92.1% chance of the next period being a circular if the current period is a circular. It is followed by linears and curvilinears, which are also relatively consistent at 80.0% and 75.3% respectively. Cluster 4, or the eclectics, as expected, are very unstable, with a consistency of only 39.6%. Cluster 4 seems to act as a sort of intermediate, since there is a substantial chance of the eclectics converting to linear (34.5%) or to a lesser degree circular (15.0%) or curvilinear (10.7%). The

transition probability between circulars and linears and vice versa is the lowest and almost nonexistent, at 0.3% and 0.2% respectively. Linears, curvilinears, and circulars rarely convert into eclectics with a probability of 12.3%, 7.5%, 5.8% respectively (and when they do, it is most likely due to collisions or using eclectics as an intermediary). This analysis provides an ethnogram of Anthrobot behavior and reveals that the most stable configuration for a spheroid is circular, followed by linear/curvilinear. The eclectics act more like an intermediate and at least probabilistically, over time, should mostly resolve into one of the 3 other categories. Therefore, we conclude that the vast majority of Anthrobot movements can be broken down into simpler, highly consistent patterns like linear, circular, curvilinear, with eclectics acting as a transient intermediary. The fact that Anthrobots exhibit movement types with high "consistency" and low rates of inter-type conversion (e.g., circulars and linears) suggests that Anthrobots self-organize into discrete movement types, each with a distinct motility fingerprint.

Anthrobots self-organize into distinct morphological types

Having observed several distinct movement classes, we next asked whether the range of their structural properties was continuous or distributed as discrete characters[56–59]. This question is important for both understanding the meso-scale rules of self-assembly, and for future efforts to control their functional properties. We hypothesized the primary parameters of this possible underlying morphological framework to be a function of the Anthrobots' 3D shape and cilia pattern, since Anthrobot motility is generated by cilia. We collected 3-dimensional structural data (Figure 3-a.1) specifically for shape and cilia layers from ~350 Anthrobots using ICC/IF and confocal microscopy and binarized these data (Figure 3-a.2) to extract quantitative information on cilia localization pattern and body boundaries. We then pipelined this information for ~350 Anthrobots into an 8-dimensional PCA cloud (Figure 3B) wherein each dimension represented a specific morphological index that we developed to quantitatively describe and characterize the Anthrobot shape and cilia patterns (See Supplemental Figure 2A).

These 8 formal morphological indices included shape-related characteristics, such as the ratio between the longest and shortest distance within a spheroid (i.e., "aspect"), longest distance within a spheroid (i.e., "max radius"), how invaginating or protruding the spheroid surface is (i.e., "shape smoothness"); as well as the cilia-related indices, such as total area covered by cilia signal on a spheroid surface ("cilia points"), cilia signal per unit area on a spheroid surface ("cilia points/area"), proximity of current cilia point distribution to a complete random uniform distribution ("cilia distribution homogeneity"), how clustered the cilia are on a spheroid surface ("polarity"), and how many free-floating cilia points there are that are not a part of a cluster ("noise points"). See Methods section for more details on how these morphological indices were calculated.

Next, we ran an unsupervised clustering algorithm on this 8-dimensional PCA cloud and observed the emergence of three statistically distinct clusters (Figure 3C), each representing a distinct morphological type (morphotype). Figure 3D shows a quantitative characterization of each cluster along 8 different morphological indices. This analysis revealed the following two characteristics to be the most important (to an equal degree, both ranking the top place in PC1 contributions) distinguishing factors between different morphotypes: the size of the Anthrobot (measured by "max radius"), and the uniformity of its shape (measured by "shape smoothness"). These two most distinguishing characteristics formally describe type 1 bots to be significantly smaller in size and smoother (spherical) in its volume, while type 2 bots to be the largest and least

uniformly shaped, and type 3 to be somewhere in between the two both. (See Methods section for PC1 and PC2 contribution rankings of different indices used to uncover this hierarchy.)

At the second level of importance in distinguishing between these three morphotypes is a set of four indices (all ranking equally top place in PC2 contributions), all pertaining to cilia characterization. While the first two of these indices characterize cilia count, i.e., the density of cilia per Anthrobot (measured by "cilia points), and the density of cilia per unit area of Anthrobot (measured by "cilia points/area"); the remaining two indices characterize the pattern in which these cilia are distributed: how tightly grouped the cilia are (measured by "polarity,"), and the amount of "free-floating" ciliary patches that are not within a group (measured by "noise points"). These four indices together describe type 2 bots as being significantly more ciliated than type 1 and type 3 bots, and type 3 bots as having a significantly more polarized cilia distribution pattern (with the least amount of extra-cluster noise) in comparison to type 1 and type 2 bots (Figure 3D).

The third most important (scoring a second level rank in both PC1 and PC2) characteristic in distinguishing between the different morphotypes is a function of both the size/shape of the Anthrobot and the localization pattern of its cilia: the homogeneity of cilia distribution on the surface of the Anthrobot (measured by "cilia distribution homogeneity"). This local index is related to, but not directly anti-correlated with, the polarity index, because while cilia distribution homogeneity characterizes local neighborhood patterns, polarity (along with its supporting index "noise points") characterizes the global (entire Anthrobot-level) cilia distribution. (See Methods for more information). In this way, we obtain both a local and a global view of the cilia distribution patterns at once, and identify type 1 bots as both globally and locally homogeneous, type 2 bots as globally homogeneous but locally heterogeneous, and type 3 bots as both globally and locally heterogeneous with high degree of global polarization.

Finally, one characteristic that does not seem to be changing in any significant way between these three morphotypes is the ratio between the longest and shortest distance within a spheroid (measured by "aspect"). Although the 3 morphotypes differ significantly in terms of the volumetric regularities (measured by the shape smoothness index) as explained above, their aspect ratios are very similar.

Taken together, our morphological characterization pipeline suggest that Anthrobots self-organize into 3 major morphotypes: type 1 Anthrobots are small, regularly shaped, tightly and uniformly covered by cilia. Type 2 and 3 bots are larger, more irregularly shaped and have less tightly-knit cilia patterns, with type 3 bots featuring significantly more polarized cilia coverage. Specific examples of these morphotypes are shown on Figure 3E.

This relationship can be represented by a developmental decision tree shown on Figure 3F wherein the first "decision point" determines the Anthrobot size and shape. Accordingly, bots that are small and regularly shaped (morphotype 1) form one branch, whereas bots that are larger and more irregularly shaped (morphotypes 2 and 3) form the alternating branch. On this alternating branch a second decision point forms further downstream and determines Anthrobot cilia pattern. Anthrobots with a non-polarized cilia pattern form one branch (morphotype 2), and Anthrobots with a polarized cilia pattern form the other (morphotype 3).

<u>Distinct movement types and morphotypes are highly correlated</u>

Having observed several discrete types of movement (Figure 2) and morphology (Figure 3) emerge, we next decided to investigate whether there is a mapping between these different movement types and morphotypes of Anthrobots. To do this, we incorporated an additional level of movement-type information into the PCA analysis used for identifying the morphotypes as

discussed in Figure 3. During the initial sample collection process for this analysis, we had been able to definitively distinguish between non-motile Anthrobots (non-movers) and motile Anthrobots (movers) (Figure 1C). To further represent the movement types observed within this mover population, we randomly sampled from the set of motile subjects, targeting 30 Anthrobots that moved well enough (*i.e., displacing movers)* to assign a movement type. The selected displacing movers were collected from the two most orthogonal movement types, circular and linear, in approximately equal proportions, to cover the extreme ends of the possible movement types.
Next, we identified these non-mover and displacing mover Anthrobots within the PCA cloud presented in Figure 3 and assigned them this additional layer of information, i.e., movement type (Figure 4A) without changing anything else in our sample size or analysis workflow. In result, 62% of non-movers were identified within morphotype 1 cluster (with the remaining 38% falling into the morphotype 2 cluster). A 100% of displacing bots were identified in morphotypical clusters 2 and 3, with ~85% of linear bots being in cluster 2, and 88% of circular bots being in cluster 3. We have further computed the statistical significance of these overlaps (using the Fisher test, see Methods) and conclude that the non-movers, linears, and circulars significantly correspond with the morphotypes 1, 2 and 3, respectively.

None of the displacing bots were identified within the morphotype 1 cluster. This suggests that the movers identified within the morphotype 1 category (i.e., those data points within the morphotype 1 cluster which are <u>not</u> labeled as "non-movers") are statistically likely to be *non-displacing movers*, displaying a stationary wiggling motion. Accordingly, we conclude that morphotype 1 bots are likely to assume either non-mover behavior or wiggler behavior. This may be attributable to their spherical shape with homogeneously distributed cilia where the propulsion forces generated by the ciliary motion are more prone to canceling each other out due to the radially symmetric spherical shape, resulting in little or no movement. Accordingly, inherent noise in the system (such as small imbalances in the cilia distribution on this spherical landscape or how the bot happened to be oriented in the plate) may be sufficient to generate small amounts of movement, i.e., wiggling, but not enough to have these bots to displace. We conclude that there is a statistically significant relationship between the Anthrobots' developmental morphology and their behavior, and show visual examples of this relationship with categorical examples on Figure 4B.

This relationship can be further represented by a decision tree in the form of a Waddington Landscape – a formalism often used to characterize cell- and body-level properties by mapping out the sequential logic of decision-points in transcriptional space or morphospace[60–63]. Figure 4C shows the Waddington Landscape for the Anthrobot. The single cell at the top of the diagram represents the single cell that will develop into the multicellular Anthrobot. During this process of self-construction, the Anthrobot moves through the developmental landscape, negotiating certain points of morphological possibility to reach its final architecture. We conclude that the unique and spontaneous 3-D multicellular morphogenesis of adult tracheal cells into Anthrobots is consistent; the final form of the Anthrobot displays a degree of variability and exhibits discrete characters with easily recognizable primary features that also map on to phenotypic behavior.

<u>Anthrobots can traverse live tissues</u>

One possible use of these living machines is to manipulate other tissues, in vitro or in vivo, in future biomedical or bioengineering applications. How will biobots react to environments

different from those that their component cells face in their native configuration in vivo? Thus, Anthrobot behaviors need to be characterized not only in a bare culture dish context, and especially in environments which tracheal epithelia do not normally encounter. Having characterized their baseline movement and morphology, we decided to study the ability of Anthrobots to traverse live tissues (specifically channel-like morphologies), taking advantage of a common model system: the scratch assay in vitro[64,65]. We produced 2-D confluent layers of human neurons derived from hiNSCs, and introduced a wound by mechanically scratching away a few Anthrobot lengths-width.

Anthrobots were placed within these "neuronal wound" environments in order to characterize the dynamics of Anthrobots in this novel biological environment. Bots were allowed to traverse on their own and timelapse videos were recorded (Figure 5A, see supplemental videos 5, 6). These videos were then tracked and specific indices were calculated from the tracked files (Figure 5B). Among these indices, we characterized the degree by which bots interact with the native tissue surrounding the scar (measured by "proportion of bot on tissue"), bots' tendency to assume a circular motility profile (measured by "bot's rotational tendency"), and bots' displacement speed in traversing the scar (measured by "instantaneous velocity"). More specifically, we investigated the relationship between bots' efficiency in traversing the scar as a function of the circularity of their movement pattern (Figure 5C). We observed a significant positive relationship (slope=1.3, p=0.01), confirming our baseline assumption that although circling bots are less efficient in forward motion, they arebetter at "exploring" the scar. We have further observed that the instantaneous velocity also had a significant positive relationship with bots' efficiency in traversing the scar (slope=0.009, p=0.048 (Figure 5D), presumably due to increased collisions with the tissue. Taken together, these data reveal that Anthrobots are capable of traversing damage sites in tissues, and that bots that have a higher rotational tendency and or higher speed end up "exploring" the tear better by covering a higher percentage of the tear interface.

Having observed the behavior of these bots in scars, we focused on the interactions between scar surfaces and the bots following the edge of the scar. In order to do so, we first constrained the dataset to trajectories that could be used to further understand the relationships between the two. More specifically we focused on bots that were not extreme in their rotational tendencies and had ample contact with the scar while not being slower than 10 microns per second in speed. This enabled us to isolate the tendency of the bot to turn consistently in the same direction (measured again by "bot's rotational tendency"), the straightness of the scar wall (measured by "scar straightness") and the correlation between the trajectory and scar edge (measured by "scar-trajectory correlation"). With our constrained dataset, we saw that Gyration had a quadratic effect on scar-trajectory similarity (Figure 5E) with p=0.0167 and scar straightness a linear effect with Slope=-1.489 and p=0.049 (Figure 5F).

Remarkably, these results suggest that there is a specific range for gyration where the scar-trajectory correlation can be maximized: Anthrobots can be chosen to specifically maximize the exploration efficiency based on their gyration. Additionally, increase in the evenness of a scar (i.e., increasing "scar straightness") leads to the bot following the scar less, which suggests Anthrobots are better at traversing irregular surfaces.

<u>Anthrobots can promote regeneration in live tissue wounds</u>

One of the most important aspects of exploring synthetic morphogenesis is the opportunity to observe novel behaviors that are obscured by standard, default phenotypes. Having seen that these tracheal cell-derived constructs can traverse and settle in neural wounds, we decided to check

for the effects of their presence on the surrounding cells. A characterization of their wild-type capabilities is important not only for understanding biological plasticity but also for establishing a baseline for future efforts in which biobots are augmented with additional synthetic circuits for pro-regenerative applications.

We first facilitated random self-aggregation of distinct Anthrobots to larger "superbot" assemblies. We accomplished this without using molds or any other external shape-giving equipment, but by simply constraining multiple Anthrobots in a relatively smaller dish, while keeping everything else constant. We then carefully placed these superbots into arbitrary sites along the tissue tear such that they span the entire width of the tear, enabling them to "bridge" two sides of the damaged tissue. Figure 6A shows a superbot on a scarred live tissue upon its placement on day 0, as well as the resulting bridge configuration on subsequent days of day 1 and day 2.

Strikingly, within the next 72 hours upon inoculation of the superbot into the tissue tear on day 0, we observed a substantial regrowth of the native tissue taking place, resulting in the formation of a stitch right underneath the "superbot bridge," connecting the two sides of the scar (Figure 6B). This stitch was observed solely at the site of superbot inoculation, and at no other place along the long tear (Figure 6C). A quantitative analysis (Figure 6D) of these self-stitch sites shows that while the neuron pixel coverage density of the stitch is as high as the native tissue outside the wound (see Supplemental Figure 3), the rest of the scar space, whether adjacent or far, had significantly less density of coverage. Thus, the density of the induced stitch area that was built with the aid of our bots represented full (statistically indistinguishable from 100%) recovery of the original tissue, and was uniquely different from the surrounding "scar" area: Anthrobot assemblies induce efficient healing of live neural tissue.

Discussion

Biorobotics and bioengineering have at least two main areas of impact. One is the production of useful living machines[27–29]. The other is the use of unconventional configurations for living materials at all scales, to probe the meso-scale rules of self-assembly of form and function[66,4,17,67]. Specifically, by confronting evolved systems with novel contexts, we can learn about the degree of plasticity that cells and control pathways can exhibit toward new anatomical and functional endpoints, as well as develop protocols to alter default outcomes. Here, we used human patient cells to begin the journey toward immunologically-acceptable, active, living biomedical constructs, and to begin to probe the morphological and functional capabilities of mammalian, adult cells.

Self-motile, fully-organic biobots have been demonstrated with frog cells[41,40,39]; however, it was unknown whether their properties depend strongly on their amphibian genome and evolutionary history, as well as their embryonic state. Moreover, their construction depended on a rate-limiting process of extracting source cells from frog embryos. Here we show a protocol for enabling the self-assembly of Anthrobots: organoids made from epithelial cells that traverse aqueous environments. The process is highly scalable, and produces Anthrobots in the course of 3 weeks, with minimal manual input, but weekly media changes. At the end of their 4-6 weeks life span, they safely degrade. Airway organoids with apical out tissue organization have very recently been shown using alternative approaches involving additional steps[43,44], but these platforms have to date been used as organotypic cultures, and have not been shown to translocate or self-organize into distinct movement or morphological types.

Anthrobots' overall shape and behavior are similar to that of Xenobots, but not identical. Anthrobots are around 20 to 300+ micrometers in size, whereas Xenobots range from an average of 487 ± 39 μm for the smallest cut explants to 602 ± 30 μm for the largest[40]. Xenobots likewise offer discrete motion types, and their behavior transition profile is similar. The interconversion between linear and circular is very small for Xenobots (0.5% and 1.6%) and Anthrobots (0.2% and 0.3%), while their consistency of Circular behavior is extremely high for Xenobots (95%) just like for Anthrobots (92%). However, Xenobots′ linear behavior consistency was not as high (67%) when compared to Anthrobots (80%). Despite their highly divergent genome, age, and tissue origin, the two platforms assemble into very similar types of creatures, illustrating the importance of generic laws of morphogenesis[8,68–72] in addition to species-specific genomic information.

Anthrobots are derived from adult human tissue, and in the future could be personalized for each patient, enabling safe in-vivo deployment of these robots in the human body without causing inflammation or triggering an immune response. Once inoculated in the body via minimally invasive methods such as injection, various applications can be imagined, including but not limited to clearing plaque buildup in the arteries of atherosclerosis patients, bulldozing the excess mucus from the airways of cystic fibrosis patients, and locally delivering drugs of interest in target tissues. They could also be used as avatars for personalized drug screening[73] having the advantage of behavior over simple organoids, which could be used to screen for a wider range of phenotypes.

Anthrobots exhibit several distinct movement and morphological classes, which are significantly correlated. This is especially important because the structure and function of this novel construct is not that of a familiar organism (despite a wild-type genome), and it was not yet known whether its morphospace possessed specific attractors, how reliable the cells' navigation of that morphospace was, or how the movement patterns would relate to its specific morphology. Anthrobots showed clear and consistent active movement types, quantified over 30 second periods: circulars, linears, curvilinears, and eclectics, with the last category including the non-displacing bots, i.e., wigglers, as well as distinct morphotypes that are best distinguished by Anthrobot size, shape, and cilia localization patterns. While more work needs to be done to establish a causal relationship between these morphotypes and the movement types, our correlation analyses showed significant correlation between the non-displacing (wiggler or non-mover) movement type and morphotype 1, linear movement type and morphotype 2, and finally circular movement type and morphotype 3. Such correlation has implications for future control of higher-order behaviors (such as movement types) by way of controlling Anthrobot morphology through synthetic morphogenesis, as well as real-time physiological signaling.

While the motion type is likely influenced by their structure, it is also likely (given the active nature of ciliary propulsion in other[74,75]) that some degree of real-time behavioral control exists. We do not yet know the degree of sophistication of the mechanisms linking environmental inputs to behaviors, and this will be tested in subsequent work where these epithelial cells will be exposed to a wide range of stimuli to which they may naturally respond. Future work will interrogate both the Anthrobots and cells in their environment (e.g., the neural scar cells) to determine whether transcriptional, physiological, or biomechanical signals are exchanged.

Like Xenobots, these are a biorobotics platform[76], in addition to a kind of organoid, because they offer an ideal model system in which to explore guided self-assembly and controlled function via future addition of metabolic and computational transcriptional circuits[5,9,77–87]. In recent years, many types of robots, mostly non-organic, have been engineered to perform operations in smaller biological contexts (millimeter or even micrometer level). Sizes of these robots have ranged from

less than a hundred micrometres[88] to insect-sized[89] at around <20 mm. Comparatively, Anthrobots fall at the lower edge of this spectrum, with sizes mostly around or below 100 microns and comparable to a "microscopic robot"[88]. Most other bots that are biologically inspired but non-organic tend to have sizes that are visible to the naked eye with microbots having a diameter ~260 micrometers[90], and crab-inspired robots around 500-700 micrometers[91] are thus a few times the size of an average Anthrobot. Other bots have had larger sizes, like the magnetically controlled soft-body milirobot ~3.7 mm [92], the water droplet manipulating magnetic-actuated robot ~ 2.4 mm[93] and the origami milirobot ~6-8 mm[94] of which the largest was the aforementioned insect-inspired robot with a size of <20 mm=20000 micrometer[89], which is tens to hundreds of times the size of the Anthrobots. Like many modern robotics platforms, they are not single-scale, deterministic, human-programmed, inorganic devices[95–101], but instead offer a tantalizing mix of baseline competencies that could eventually be managed and augmented by environmental stimuli and the addition of smart materials, circuits, and behavior-shaping protocols.

As has been seen in evolutionary robotics in artificial life and computer engineering[102], these offer surprises. In many ways, characterizing these constructs resembles studying a new organism, because novel properties abound despite its familiar (wild-type human) genotype. The most amazing to date is their ability (Figure 6) to induce the healing of neural scars. This capacity for tracheal cells (like their propensity to reboot their multicellularity into a motile spheroid) could not have been predicted from first principles, and we hypothesize that numerous other surprising abilities remain to be found in the future. This offers many implications for therapeutics, not only in the direct use of Anthrobots on neural wounds but in the extension of this principle to optimize other kinds of biological repair-inducing constructs.

These data establish a research program with many unanswered questions for subsequent work. What other cells can Anthrobots be made of? What other behaviors might they exhibit, and in what environments? What other cell types can they repair or affect in other ways? Can transcriptional or physiological signatures be read out in living bots, that reflect their past and immediate interactions with surrounding cellular or molecular landscapes? Do they have preferences or primitive learning capacities[103], with respect to their traversal of richer environments? More fundamentally, these data reveal additional morphogenetic competencies of cells which could have implications for evolutionary developmental biology, as evolution of anatomical and functional features could be affected by the ability of the same genome to produce very diverse forms in different environments. Finally, this kind of new model system is a contribution to two key future efforts. The study of synthetic biological systems[11,104,17,105] is an essential complement to the standard set of phenotypic defaults available in the natural phylogenetic tree of Earth, revealing the adjacent possible in morphological and behavioral spaces[106,107]. Moreover, these systems offer a safe, highly tractable sandbox in which to learn to predict and control the surprising and multi-faceted system-level properties of multiscale complex systems.

Methods

NHBE culture

Normal human bronchial epithelial cells (NHBE) were used from Lonza Walkersville, MD. The cells were first thawed and seeded on a T150 flask containing bronchial epithelial growth medium (Lonza CC-3170) for 2D cell culture growth. Once the NHBEs were ~80% confluent, they were passaged into a 24-well-plate of Matrigel beds for 3D cell culture. The NHBEs were not passaged past the 3rd passage. Each matrigel bed contained 500µL of 25% Matrigel-, 0.1% 0.5nM retinoic acid and 75% BEDM that was centrifuged for 5 seconds at 100 x g and prepared at least 4 hours before passaging the cells. The cells were re-suspended in 5% matrigel, 95% BEDM and 0.1% RA and seeded directly onto the matrigel beds with 500µL per well at a 30,000 cells/mL concentration. Once seeded, the NHBEs were centrifuged for 5 seconds at 50 x g. On days 2 and 8, the NHBEs received a top feed containing 750µL 5% matrigel, 95% BEDM, and 0.1% RA. On day 14, 500µL of the wells' contents was aspirated and 500µL of dispase (#D469) at concentration 2 mg/mL was added to each well. A mini cell scraper was used to break up the matrigel clumps and then followed by a 0.05% Triton coated pippete tip to mix up the matrigel with the dispase. The dispase was then incubated at 37°C for 1 hour with the pipetting process repeated every 15 minutes. During incubation, Pluristrainer Mini's with a 40 µm pore size (Fisher Scientific #431004050) were placed in wells of a fresh 24-well-plate that contained 2.5 mL of 0.05% Triton. After the incubation period, 250 µL of 1% 5mM EDTA in D-PBS was added into each well. The media in each well was then drawn up, using the Triton-coated tip, and added to the Triton-coated strainers. The NHBE spheroids in the strainer were rinsed with 1 mL of D-PBS then expelled onto a low adhesive dish by inverting the strainer over the dish and expelling 5 times of 1 mL of BEDM through the bottom of the strainer. After all spheroids were in one dish, they were divided evenly amongst multiple 60mm dishes by using a Triton-coated pipette tip and a microscope to manually draw up and divide them. 0.5µL of 0.5nM retinoic acid was added into each dish once divided. For the next 14 days as the spheroids started moving, they required 0.5µL of 0.5nM retinoic acid every other day and a media change every 4 days. The media change was performed by circling the Anthrobots to the center of the dish then collecting 2 mL of old media and adding 3 mL of fresh BEDM-this was done under a microscope to ensure no Anthrobots got aspirated.

Neuronal culture

A 150 cm dish was first coated with 0.1% gelatin for 20 minutes and then aspirated off before seeding mouse embryonic fibroblasts (ATCC #SCRC-1008) in MEF growth media (89% DMEM GlutaMAX, 10% Fetal Bovine Serum, and 1% Anti-anti). Once the MEFs were confluent, they were inactivated by adding 20 mL of MEF growth media containing 500 µL of 10µg/mL mitomycin C (Sigma #M4287) and incubating for 2-3 hours at 37°C. After incubation, the MEF growth media + mitomycin C media was replaced with hiNSCs at a density of 1/10 of a confluent target vessel in 25 mL of hiNSC growth media (77.6% Knockout DMEM, 20.20% KOSR, 1% GlutaMAX, 1% Anti-anti, 0.18% 2-mercaptoethanol with 0.1 % of 20 ng/mL bFGF). The day after seeding the hiNSCs required a media change where all the old media was aspirated off, and 25 mL of fresh hiNSCs growth media was added. Media changes were performed every other day until the hiNSCs were 80-85% confluent. 3 hours before performing the differentiation, the destination vessels were first coated with .1mg/mL poly-d-lysine (enough to coat the bottom of the wells) for one hour at room temp, and then the PDL was aspirated before adding in 10ug/mL laminin in DPBS (enough to coat the bottom) for 2 hours at 37°C. In the differentiation, the hiNSCs

first went through one D-PBS wash before adding TrypLE Select for 3-5 min to detach the cells from the plate. The cells were then collected and spun down for 3 minutes at 500g then resuspended in neurobasal differentiation media (96% Neurobasal Media, 2% B-27 supplement, 1% GlutaMAX, 1% Anti-anti). The hiNSCs were seeded at a concentration of 100,000 cells/cm^2. Once the hiNSCs were in differentiation, there was a media change the day preceding their differentiation and then every other day from there .

Immunocytochemistry / Immunofluorescence

Anthrobots were collected in Pluristrainer Mini's with a 40-micron pore size (Fisher Scientific #431004050) and fixed with 4% paraformaldehyde at room temperature for 30 minutes. Following PBS washes, blocking and permeabilization were performed for 1 hour at room temperature on a rocker in a blocking buffer consisting of phosphate-buffered saline with 10% normal goat serum, 1% bovine serum albumin, and .15% triton x-100. Anthrobots were then incubated with mouse anti-acetylated tubulin (Sigma-Aldrich #T7451) and rabbit anti-cytokeratin 5 (Abcam #ab52635) primary antibodies diluted 1:250 and 1:100, respectively, in blocking buffer for 24 hours at 4oC on a rocker. The primary antibodies were labeled with Alexa Fluor 647 donkey anti-mouse (Thermo Fisher Scientific #A31571) and Alexa Fluor 488 donkey anti-rabbit (Abcam #ab150073) secondary antibodies, both at 1:500 dilutions in blocking buffer, for 1 hour at room temperature on a rocker. Lastly, Anthrobots were incubated with Alexa Fluor 594-conjugated mouse anti-ZO-1 (Thermo Fisher Scientific #339194) at a 1:100 dilution in blocking buffer for 24 hours at 4oC on a rocker. Anthrobots were mounted on glass-bottom 96-well plates in ProLong Glass Antifade Mountant with NucBlue (Thermo Fisher Scientific #P36981). Images were collected using a Lecia SP8 FLIM microscope with a 25x water immersion objective. Z-stack step size=3 micron unless otherwise specified.

Tracking timelapse videos

Timelapse videos of the Anthrobots were contrast-enhanced using the video editing software ImageJ. They were then processed to extract the trajectories of the Anthrobots utilizing the trackR function in the trackR package (version 0.5.1) for R. The software parameters were chosen manually in order to increase the accuracy of the tracking, following the instructions in the trackR package's help. Tracking errors such as the swapping, deletion or insertion of tracks were subsequently manually corrected using the trackFixer function from the same package.

Movement type analysis

From the extracted trajectories, we computed the following metrics: (i) the linear distance between the current position and the immediately preceding one; (ii) the linear speed at each position, approximated as the distance moved between the current position and the immediately preceding one during the time interval between these two positions; (iii) the heading of the bot at each position, approximated as the angle between the vector formed by the current position and the immediately preceding one and that formed by the current position and the immediately following one; (iv) the angular speed of the bot at each position, approximated as the difference between the heading at the immediately preceding position and that at the current one during the time interval between the corresponding three positions required to calculate these two headings; (v) the time difference between each position.

Behavioral classification was then performed on non-overlapping 30-second blocks of trajectory. To determine how predictable a position change was, the linear speed, heading, and

angular speed were estimated at each position to predict the coordinates of the following position. The error (Euclidean distance) between the predicted coordinates and the actual coordinates was then computed. For each complete 30-second block of trajectory (i.e., a block with no missing timestamp), total error over the entire block was calculated and normalized by the total distance traveled during that block to account for the artificial error amplification caused by predicting over longer distances. To separate active from inactive blocks, an automated classification method was used on the distribution of total normalized errors. A gamma mixture model with two components was fit to the data using the expectation maximization algorithm in the REBMIX function from the rebmix package (version 2.12.0) for R[108]. The 30-second periods in the resulting cluster with the highest total normalized error were considered as inactive and excluded from further classification.

We then derived two metrics to describe each trajectory: (i) a "straightness" index computed as 1 minus the circular variance of the headings during the block (a value of 1 indicates a perfectly straight line) and (ii) a "gyration" index computed as 1 minus the circular variance of the angular speed during the block divided by the circular variance of the same angular speeds and their additive inverse, which helps in taking into account the magnitude of the angular speeds themselves (a value of 1 indicates a trajectory following a perfect circle).

The need for two indices arises from the fact that a straightness index alone cannot fully tease apart all different movement types due to its aggregate view of a trajectory. In other words, a low straightness index does not automatically translate into a perfectly circular bot, as we can see in Supplemental Figure 1-a.1 and 1-a.2 with the arc trajectory. This is due to the fact that the straightness index does not account for the time-dependent dynamics and thus ignores individual variations across frames. This is where the second movement metric, the gyration index, comes into play. To account for temporal information, we calculate the angular speed, which is the difference between successive headings divided by time between frames and thus has units of radians/ second. Supplemental Figure 1B shows a bent trajectory and Supplemental Figure 1C shows an arc trajectory, both of which have similar straightness indices. However, when we start looking at their temporal relationships using angular speeds, the behavior is entirely different. For the arc (Figure S1C), the variance of the angular speed is very small since the change in heading of the trajectory each time is relatively consistent (the distribution shown in the histograms).

For the bent trajectory (Figure S1B), the variance of angular speed is much larger than the arc since for most of the trajectory the angular speed is close to 0 (it goes straight), but the bent portion has a very high angular speed, i.e., the angle changes very quickly. In general, the greater the absolute value of the angular speed the sharper the turn in the trajectory (zero is straight) and the greater the variance of the angular speeds, the less the consistency of the turns in the trajectory. A circle or arc usually has absolute values of the angular speed much greater than zero and low variation of angular speed. However, the gyration index alone cannot differentiate between all behavior either. Let's look at a circular trajectory (Supplemental Figure 1D). Even though the absolute values of the angular speeds between arcs and circles are different, the circle also ends up having a gyration index close to 1 since all the turns in a circle are highly consistent like in an arc and thus the variance of the angular speed for both is very small. This fact means the gyration index cannot segregate between arcs and circles, among other things, by itself. Interestingly, the straightness index is exceptional at separating arcs and circles. This shows that though either index alone cannot distinguish all movement types well, together they can accomplish much more.

To separate the trajectory blocks into categories of similar behavior after calculating the movement metrics, a cross-entropy clustering algorithm was used[109], and implemented in the cec

function of the CEC package (version 0.10.2) for R[110]. This yielded us six categories, of which trajectories from categories numbered 3 and 4 were merged into categories numbered 1 and 2 respectively due to the difference being phenotypically minimal. In the "behavioral space" as defined by the straightness and gyration indices, cluster 3 had the same straightness index range as cluster 1 and a lower gyration range between roughly 0.65 and 0.95, which represented trajectories that were highly circular but fell short of cluster 1 which represented "prototypical circulars". Similarly, Cluster 4 had a slightly smaller straightness index range than cluster 2 (0.7 to 1 instead of 0.6 to 1) and higher gyration range between 0.1 and 0.55 which represented trajectories that were mostly linear but didn't have a high enough gyration to be curvilinear or low enough gyration to be Cluster 2, a "prototypical linear". The merge of the two clusters increased the average dissimilarity of the cluster, but it is a testament to how similar clusters 1 and 3, and 2 and 4 were already that their dissimilarity still remains very low at ~0.09 and ~0.14 respectively. Last, to understand how the bots' behaviors are distributed relative to each other, transition probabilities between each behavioral category were estimated by calculating the proportion of times a block of a given category is followed by a block of the same or another category. This was then presented in the form of a Markov Chain.

Morphotype analysis

To find whether there were any unique morphological types like was the case with movement types, each spheroid was processed through a custom-made analysis pipeline (code attached). First, we created a 3D model of the bot in R where the points corresponding to the body and the cilia were clearly indicated. For this, we first isolated the cilia channel from the LIF images of the bots and ran the images through CiliaQ[111] using the RenyiEntropy algorithm for detection. These binarized cilia were then imported into our code, along with the points that comprised the body. These "body points" were extracted using the "body channel" of the LIF images by first running the pixels through a logistic transform then thresholding the pixels based on the signal to noise ratio, calculated by using a median filter and comparing the points before ("signal + noise") to after ("only signal").

Due to the large volume of body points, to reduce the points to a manageable amount, we found outlines of each slice of the spheroid by using a concave hull using the Concaveman package (version 1.1.0)[112]. The cilia points were then projected on the nearest body points by simply choosing the nearest one by distance to get the shadow of the cilia on the body.

The structural index variable Cilia Points was calculated by counting the number of unique projected points on the body. Then, the dbscan package (version 1.1-10)' [113]function in R was used to find the clusters of cilia. The number of points that fell outside of clusters with this definition were defined as Noise Points.

Following this step we computed the spanning ellipsoid of the body points by using the 'ellipsoidhull' function from the cluster package (version 2.1.3)[114]. The Max Radius variable was calculated directly by the function, and Aspect was defined as the ratio of the largest radius to the shortest radius, all quantities computed by the function. Finally, we used the 'ashape3D' function from the alphashape3d package (version 1.3.1) [115] to generate a 3D alpha hull of the body points, and used the mesh to get the surface area of each spheroid.

Cilia Points/Area was defined as the Cilia Points variable divided by the calculated surface area. Similarly, the Shape Smoothness was defined as the ratio of the volume of the 3D alpha hull to the volume of the spanning ellipsoid. Finally, we found the center of the bot by finding the sum of the centroids of each triangle that makes up the alpha hull weighted by area of the triangle. Polarity was defined as the norm of the vectors from the center to each cilia point divided by the sum of the norm

of each vector. The Cilia Distribution Homogeneity was defined as 1 - D statistic of the two sample Kolmogorov-Smirnov test, where sample A is the 1st nearest neighbor (1NN) distances for the cilia, and sample B the 1NN distances if the same number of cilia points were distributed close to uniformly but randomly across the surface of the bot. After these analyses were carried out, we ran the dataset through a Principal Components Analysis with centering and scaling. Afterwards, a hierarchical clustering was carried out on the resultant dataset with the Ward.D2 method and the resulting classification was plotted as above. In total, 350 bots were put through the pipeline and into the following PCA and included Movers, Nonmovers, Linears and Circulars. Further details can be seen in the code.

To get a confidence interval for the absolute value of the loadings, we bootstrapped the loading value by sampling 250 bots from the 350 that we have, 10 times. We then took the loadings value for the 1st and the 2nd primary component for all 8 variables and calculated the mean and 95% Confidence Interval for the loadings for the PC in question. If there was overlap between the CI of the loadings, they were assigned the same rank, otherwise they were assigned different ranks. Ranks were relative to the "highest" contributor of the rank; i.e, for PC1, Shape Smoothness had overlap with Max Radius, but it also had overlap with Cilia Distribution Homogeneity. However, Cilia Distribution Homogeneity did not overlap with Max Radius. Max Radius had the highest upper limit of the CI among the 3 variables in question, and thus Shape Smoothness was co-ranked #1 along with Max Diameter, but Cilia Distribution Homogeneity was not.

Morphotype & movement type overlap

After finding trends among behavioral and morphological data, we decided to see if there was any potential overlap between the two. To eke out any possible correlation, we first chose to use categories of spheroids behaviorally orthogonal to movers, the non-movers. The goal was to observe whether there is any overlap between the morphology of movers and non-movers. Similarly, we had four potential behavioral types that could overlap with our morphological clusters. Eclectics could not be included in the analysis since they are an aggregate of multiple inconsistent patterns and highly uncommitted to their behavior (Figure 2G), and thus cannot be used in a bot-level analysis (instead of period). Circulars and Linears on the other hand were highly committed behavioral types that were orthogonal to each other (had little to no interconversion on the Markov plot) and prototypes of two extreme movement types with high variability between them. Consequently, the Curvilinear behavioral subtype was also not included since it lacked orthogonality with both Circulars and Linears due to shared traits between them. The morphological indices for each spheroid were calculated as outlined in the methods for the previous sections, and then clustered with Circulars, Linears, Nonmovers and Movers together. To measure the significance of the overlap, if any, between clusters, we decided to use a Fisher test to compute whether the proportion of a certain behavior per cluster type was different from the others. We ran the test twice, once to see if there were any significant differences in number of nonmovers per cluster, and once to compute the difference in the ratio between circulars and linears per cluster. It showed that the proportion of nonmovers in Cluster 1 vs. Clusters 2 and 3 were significantly different with an average $p=2.6*10e-6$ and $3.5*10e-8$ respectively Cluster 2 and 3 also had a statistically significant difference in number of nonmovers ($p=0.01$) which is understandable, since Cluster 2 had no non-movers. For Circular/Straight, Cluster 2 vs. 3 were significantly different with $p=0.00011$, and Cluster 1 had no Circulars nor Straights.

Traversal video tracking and analysis

To better explain the relationship between bot trajectory and movement in certain environments, we tried to relate the scar edge to the actual movement of the bot. The steps taken before analysis involved (i) creating a background image prototype from the.czi recording, (ii) verifying the quality of the background image and saving as .png file, (iii) tracking the bot, (iv) extracting the coordinates of the scar, and (v) checking whether tracking was correctly carried out by generating a video with a beacon on the bot.

This procedure was carried out on 30+ files and yielded 21 usable datasets, which were whittled down to 12 after a manual check of quality. Using the coordinates of the scar walls and the tracking of the bot, we used the Rbioformats (version 0.0.74)[116] and Rvision (version 0.6.2)[117] package tools to test (1) whether bots are more in contact with the scar when they have a higher rotational tendency and (2) when moving on tissue, whether faster bots tend to cover more area i.e., explore better. The lm() function was used to model the data after calculation of proportion of bot on tissue, instantaneous angular velocity and linear speed as variables. Before each model was approved, diagnostics were run on the model using the DHARMa package which included analysis of the residuals.

Afterwards, in order to take a better look at the nuances of interactions between bots and scars, we decided to limit the data and remove any videos that had an average linear speed of less than 10 microns per second because they were moving too slowly for the effect of the scar on movement to be truly studied since they didn't traverse enough of the scar. Additionally, bots with very low rotational tendency (=<~0.3) were excluded since they were not stable enough in their rotational behavior. Finally, bots with either very high rotational tendency (>=0.7) and low angular velocity (which means the bot was "skidding") or bots with low levels of overlap/contact with scar were removed. After all these removals, our dataset ended up with 6 examples of scar-bot interactions which could be effectively analyzed. In order to calculate the Scar Straightness, the distance between the two endpoints from the section above were divided by the sequential from left to right sum of the distances of the points. The Gyration was simply the Rotational Tendency values renamed. Our Scar-Trajectory Similarity metric was calculated as the larger absolute value of the correlation between the heading angle of the trajectory and the heading angles of the scar from the surface perpendicular to the bot. These correlation values were then modelled using the lm() function with an expectation of a quadratic relationship for Gyration and a linear one for Scar Straightness. The specifics can be seen in the attached code.

Traversal Video Processing

Traversal videos of bots moving along a scar within a neuron plate were processed via Adobe Illustrator to see if the bot faithfully followed the edge of the scar. The videos were processed within Adobe Photoshop to generate image sequences compatible with Illustrator for this analysis. The first method of processing aligned the center of the scar at a horizontal line parallel to the bottom of the screen and placed a point on the center of the bot at each frame of the video as well as straight above and below this point on the edges of the scar. Lines were made to connect each respective type of point for both of the edges of the scar and the position of the bot. The output of this for further analysis was a set of coordinates of the end of each line derived from rendering these series of lines as an SVG file and exported as text.

Neuronal tissue density analysis

To investigate whether these "bridges" were actually akin to neurons, we decided to analyze the pixel densities of various areas on and surrounding the bridge. In order to prevent confusions regarding this process with regard to intensity of color, we to binarized the image on ImageJ. If the automatic thresholding did not visually appear similar to the raw image, we adjusted the threshold manually. We ended up with six areas of interest: the neurons above the bridge, below the bridge, to the left but adjacent, to the left but far, and to the right, both adjacent and far. These areas were defined relative to a FIJI ROI box on the neuronal bridge which tried to encompass the width of the bridge and the height close to the narrowest point of the scar channel that we would interact with. A line of one bridge length or lower if the image size required smaller lines to fit the boxes was used in the vertical and horizontal directions (called hereafter as "bridge length"). The above and below bridge measurements were taken by placing the bounding box one vertical bridge length from the box on the neuronal ridge. The adjacent areas on both sides were defined as 1 horizontal bridge length away from the bridge in the scar. The far areas were 1 bridge length beyond the adjacent areas. The far and adjacent boxes were (vertically) adjusted so they overlaid the scar as much as possible (Figure S6). Finally, we used Analyze>Histogram in FIJI to get the size of the box (which was constant) and the number of pixels of scar tissue (in black) and calculated the proportion. We then used an unpaired two sample T-test with unequal SD to calculate the significance of the difference, if any.

Acknowledgements

We thank Santosh Manicka for helpful technical discussion of Multivariate Classification, Roger Kamm and David Kaplan for in-vitro bot inoculation discussion. We also thank Doug Blackiston, Joshua Bongard, Caitlin Grasso and Sam Kriegman for high-level scientific discussions, and Julia Poirier for helpful comments on the manuscript. M.L. gratefully acknowledges support via grant 62212 from the John Templeton Foundation.

References

1. Pezzulo, G. & Levin, M. Re-membering the body: applications of computational neuroscience to the top-down control of regeneration of limbs and other complex organs. *Integr. Biol.* **7**, 1487–1517 (2015).
2. Abramson, C. I. & Levin, M. Behaviorist approaches to investigating memory and learning: A primer for synthetic biology and bioengineering. *Commun. Integr. Biol.* **14**, 230–247 (2021).
3. Fields, C. & Levin, M. Competency in Navigating Arbitrary Spaces as an Invariant for Analyzing Cognition in Diverse Embodiments. *Entropy Basel Switz.* **24**, 819 (2022).
4. Davies, J. A. & Glykofrydis, F. Engineering pattern formation and morphogenesis. *Biochem. Soc. Trans.* **48**, 1177–1185 (2020).
5. Solé, R. Synthetic transitions: towards a new synthesis. *Philos. Trans. R. Soc. B Biol. Sci.* **371**, 20150438 (2016).
6. Ollé-Vila, A., Duran-Nebreda, S., Conde-Pueyo, N., Montañez, R. & Solé, R. A morphospace for synthetic organs and organoids: the possible and the actual. *Integr. Biol.* **8**, 485–503 (2016).
7. Arias Del Angel, J. A., Nanjundiah, V., Benítez, M. & Newman, S. A. Interplay of mesoscale physics and agent-like behaviors in the parallel evolution of aggregative multicellularity. *EvoDevo* **11**, 21 (2020).
8. Newman, S. A. 'Biogeneric' developmental processes: drivers of major transitions in animal evolution. *Philos. Trans. R. Soc. B Biol. Sci.* **371**, 20150443 (2016).
9. Andrianantoandro, E., Basu, S., Karig, D. K. & Weiss, R. Synthetic biology: new engineering rules for an emerging discipline. *Mol. Syst. Biol.* **2**, (2006).
10. Teague, B. P., Guye, P. & Weiss, R. Synthetic Morphogenesis. *Cold Spring Harb. Perspect. Biol.* **8**, a023929 (2016).

11. Davies, J. A. Synthetic morphology: prospects for engineered, self-constructing anatomies: Synthetic morphology, J. A. Davies. *J. Anat.* **212**, 707–719 (2008).
12. Santorelli, M., Lam, C. & Morsut, L. Synthetic development: building mammalian multicellular structures with artificial genetic programs. *Curr. Opin. Biotechnol.* **59**, 130–140 (2019).
13. Johnson, M. B., March, A. R. & Morsut, L. Engineering multicellular systems: Using synthetic biology to control tissue self-organization. *Curr. Opin. Biomed. Eng.* **4**, 163–173 (2017).
14. Ho, C. & Morsut, L. Novel synthetic biology approaches for developmental systems. *Stem Cell Rep.* **16**, 1051–1064 (2021).
15. Hoffman, T. *et al.* Synthetic Biology and Tissue Engineering: Toward Fabrication of Complex and Smart Cellular Constructs. *Adv. Funct. Mater.* **30**, 1909882 (2020).
16. Aydin, O. *et al.* Principles for the design of multicellular engineered living systems. *APL Bioeng.* **6**, 010903 (2022).
17. Ebrahimkhani, M. R. & Ebisuya, M. Synthetic developmental biology: build and control multicellular systems. *Curr. Opin. Chem. Biol.* **52**, 9–15 (2019).
18. Toda, S., Frankel, N. W. & Lim, W. A. Engineering cell–cell communication networks: programming multicellular behaviors. *Curr. Opin. Chem. Biol.* **52**, 31–38 (2019).
19. Gumuskaya, G. Form From Within: Scaling Up Self-Constructing Biological Architectures through a Novel Application of Synthetic Morphogenesis. (Massachusetts Institute of Technology, 2018).
20. Morsut, L. *et al.* Engineering Customized Cell Sensing and Response Behaviors Using Synthetic Notch Receptors. *Cell* **164**, 780–791 (2016).
21. Toda, S., Blauch, L. R., Tang, S. K. Y., Morsut, L. & Lim, W. A. Programming self-organizing multicellular structures with synthetic cell-cell signaling. *Science* eaat0271 (2018) doi:10.1126/science.aat0271.

22. Toda, S. *et al.* Engineering synthetic morphogen systems that can program multicellular patterning. *Science* **370**, 327–331 (2020).

23. Karig, D. *et al.* Stochastic Turing patterns in a synthetic bacterial population. *Proc. Natl. Acad. Sci.* **115**, 6572–6577 (2018).

24. Gumuskaya, G. Multimaterial bioprinting—minus the printer: Synthetic bacterial patterning with UV-responsive genetic circuits. *Int. J. Archit. Comput.* **19**, 121–141 (2021).

25. Basu, S., Gerchman, Y., Collins, C. H., Arnold, F. H. & Weiss, R. A synthetic multicellular system for programmed pattern formation. *Nature* **434**, 1130–1134 (2005).

26. Basu, S., Mehreja, R., Thiberge, S., Chen, M.-T. & Weiss, R. Spatiotemporal control of gene expression with pulse-generating networks. *Proc Natl Acad Sci U A* **101**, 6355–6360 (2004).

27. Kamm, R. D. & Bashir, R. Creating Living Cellular Machines. *Ann. Biomed. Eng.* **42**, 445–459 (2014).

28. Kamm, R. D. *et al.* Perspective: The promise of multi-cellular engineered living systems. *APL Bioeng.* **2**, 040901 (2018).

29. Ebrahimkhani, M. R. & Levin, M. Synthetic living machines: A new window on life. *iScience* **24**, 102505 (2021).

30. Doursat, R. & Sánchez, C. Growing Fine-Grained Multicellular Robots. *Soft Robot.* **1**, 110–121 (2014).

31. Doursat, R., Sayama, H. & Michel, O. A review of morphogenetic engineering. *Nat. Comput.* **12**, 517–535 (2013).

32. Ricotti, L. *et al.* Biohybrid actuators for robotics: A review of devices actuated by living cells. *Sci. Robot.* **2**, eaaq0495 (2017).

33. Menciassi, A., Takeuchi, S. & Kamm, R. D. Biohybrid systems: Borrowing from nature to make better machines. *APL Bioeng.* **4**, 020401 (2020).

34. Sakar, M. S. *et al.* Formation and optogenetic control of engineered 3D skeletal muscle bioactuators. *Lab. Chip* **12**, 4976 (2012).

35. Chan, V. *et al.* Development of Miniaturized Walking Biological Machines. *Sci. Rep.* **2**, 857 (2012).

36. Nawroth, J. C. *et al.* A tissue-engineered jellyfish with biomimetic propulsion. *Nat. Biotechnol.* **30**, 792–797 (2012).

37. Raman, R. *et al.* Optogenetic skeletal muscle-powered adaptive biological machines. *Proc. Natl. Acad. Sci.* **113**, 3497–3502 (2016).

38. Park, S.-J. *et al.* Phototactic guidance of a tissue-engineered soft-robotic ray. *Science* **353**, 158–162 (2016).

39. Kriegman, S., Blackiston, D., Levin, M. & Bongard, J. Kinematic self-replication in reconfigurable organisms. *Proc. Natl. Acad. Sci.* **118**, e2112672118 (2021).

40. Blackiston, D. *et al.* A cellular platform for the development of synthetic living machines. *Sci. Robot.* **6**, eabf1571 (2021).

41. Kriegman, S., Blackiston, D., Levin, M. & Bongard, J. A scalable pipeline for designing reconfigurable organisms. *Proc. Natl. Acad. Sci.* **117**, 1853–1859 (2020).

42. Doursat, R., Sayama, H. & Michel, O. Morphogenetic Engineering: Reconciling Self-Organization and Architecture. in *Morphogenetic Engineering* (eds. Doursat, R., Sayama, H. & Michel, O.) 1–24 (Springer Berlin Heidelberg, 2012). doi:10.1007/978-3-642-33902-8_1.

43. Wijesekara, P. *et al. Engineering Rotating Apical-Out Airway Organoid for Assessing Respiratory Cilia Motility*. http://biorxiv.org/lookup/doi/10.1101/2022.01.15.476455 (2022) doi:10.1101/2022.01.15.476455.

44. Boecking, C. A. *et al.* A simple method to generate human airway epithelial organoids with externally orientated apical membranes. *Am. J. Physiol.-Lung Cell. Mol. Physiol.* **322**, L420–L437 (2022).

45. Sachs, N. *et al.* Long-term expanding human airway organoids for disease modeling. *EMBO J.* **38**, (2019).

46. Wu, X., Peters-Hall, J. R., Bose, S., Peña, M. T. & Rose, M. C. Human Bronchial Epithelial Cells Differentiate to 3D Glandular Acini on Basement Membrane Matrix. *Am. J. Respir. Cell Mol. Biol.* **44**, 914–921 (2011).

47. Zhou, J. *et al.* Differentiated human airway organoids to assess infectivity of emerging influenza virus. *Proc. Natl. Acad. Sci.* **115**, 6822–6827 (2018).

48. Barkauskas, C. E. *et al.* Lung organoids: current uses and future promise. *Development* **144**, 986–997 (2017).

49. Co, J. Y. *et al.* Controlling Epithelial Polarity: A Human Enteroid Model for Host-Pathogen Interactions. *Cell Rep.* **26**, 2509-2520.e4 (2019).

50. Hild, M. & Jaffe, A. B. Production of 3-D Airway Organoids From Primary Human Airway Basal Cells and Their Use in High-Throughput Screening. *Curr. Protoc. Stem Cell Biol.* **37**, (2016).

51. Wiens, J. J. Character Analysis in Morphological Phylogenetics: Problems and Solutions. *Syst. Biol.* **50**, 689–699 (2001).

52. Thiele, K. The Holy Grail of the Perfect Character: The Cladistic Treatment of Morphometric Data. *Cladistics* **9**, 275–304 (1993).

53. Torres, L. G., Orben, R. A., Tolkova, I. & Thompson, D. R. Classification of Animal Movement Behavior through Residence in Space and Time. *PLOS ONE* **12**, e0168513 (2017).

54. Gonsek, A., Jeschke, M., Rönnau, S. & Bertrand, O. J. N. From Paths to Routes: A Method for Path Classification. *Front. Behav. Neurosci.* **14**, (2021).

55. Yamazaki, S. J. *et al.* STEFTR: A Hybrid Versatile Method for State Estimation and Feature Extraction From the Trajectory of Animal Behavior. *Front. Neurosci.* **13**, (2019).

56. Marramà, G. & Kriwet, J. Principal component and discriminant analyses as powerful tools to support taxonomic identification and their use for functional and phylogenetic signal detection of isolated fossil shark teeth. *PLOS ONE* **12**, e0188806 (2017).

57. Larsen, P. A., Marchán-Rivadeneira, M. R. & Baker, R. J. Natural hybridization generates mammalian lineage with species characteristics. *Proc. Natl. Acad. Sci.* **107**, 11447–11452 (2010).

58. Clemmensen, K. E. & Michelsen, A. Integrated long-term responses of an arctic–alpine willow and associated ectomycorrhizal fungi to an altered environment. *Can. J. Bot.* **84**, 831–843 (2006).

59. Santos, M. A. B. dos *et al.* Morphological Diversity of Springtails in Land Use Systems. *Rev. Bras. Ciênc. Solo* **42**, (2018).

60. Masiello, M. G., Verna, R., Cucina, A. & Bizzarri, M. Physical constraints in cell fate specification. A case in point: Microgravity and phenotypes differentiation. *Prog. Biophys. Mol. Biol.* **134**, 55–67 (2018).

61. Sato, A. Chaperones, Canalization, and Evolution of Animal Forms. *Int. J. Mol. Sci.* **19**, E3029 (2018).

62. Townsend, G., Hughes, T., Bockmann, M., Smith, R. & Brook, A. How studies of twins can inform our understanding of dental morphology. *Front. Oral Biol.* **13**, 136–141 (2009).

63. Fooladi, H., Moradi, P., Sharifi-Zarchi, A. & Hosein Khalaj, B. Enhanced Waddington landscape model with cell–cell communication can explain molecular mechanisms of self-organization. *Bioinformatics* **35**, 4081–4088 (2019).

64. Cory, G. Scratch-wound assay. *Methods Mol. Biol. Clifton NJ* **769**, 25–30 (2011).

65. Martinotti, S. & Ranzato, E. Scratch Wound Healing Assay. *Methods Mol. Biol. Clifton NJ* **2109**, 225–229 (2020).

66. Davies, J. & Levin, M. Synthetic morphology via active and agential matter. Preprint at https://doi.org/10.31219/osf.io/xrv8h (2022).

67. Velazquez, J. J., Su, E., Cahan, P. & Ebrahimkhani, M. R. Programming Morphogenesis through Systems and Synthetic Biology. *Trends Biotechnol.* **36**, 415–429 (2018).

68. Beloussov, L. V. Mechanically based generative laws of morphogenesis. *Phys. Biol.* **5**, 015009 (2008).

69. Davidson, L. A. Epithelial machines that shape the embryo. *Trends Cell Biol.* **22**, 82–87 (2012).

70. Miller, C. J. & Davidson, L. The interplay between cell signaling and mechanics in developmental processes. *Nat. Rev. Genet.* **14**, 733–744 (2013).

71. Newman, S. A. Inherency and homomorphy in the evolution of development. *Curr. Opin. Genet. Dev.* **57**, 1–8 (2019).

72. Newman, S. A. Inherency of Form and Function in Animal Development and Evolution. *Front. Physiol.* **10**, (2019).

73. Ingber, D. E. Human organs-on-chips for disease modelling, drug development and personalized medicine. *Nat. Rev. Genet.* **23**, 467–491 (2022).

74. Tamm, S. L. & Tamm, S. Ciliary reversal without rotation of axonemal structures in ctenophore comb plates. *J. Cell Biol.* **89**, 495–509 (1981).

75. Wyman, J. NEUROID TRANSMISSION IN CILIATED EPITHELIUM. *J. Gen. Physiol.* **7**, 545–559 (1925).

76. Bongard, J. & Levin, M. Living Things Are Not (20th Century) Machines: Updating Mechanism Metaphors in Light of the Modern Science of Machine Behavior. *Front. Ecol. Evol.* **9**, (2021).

77. Solé, R. The major synthetic evolutionary transitions. *Philos. Trans. R. Soc. B Biol. Sci.* **371**, 20160175 (2016).

78. Solé, R. Synthetic collective intelligence. *Biosystems* (2016).

79. Urrios, A. *et al.* A Synthetic Multicellular Memory Device. *ACS Synth. Biol.* **5**, 862–873 (2016).

80. Purnick, P. E. M. & Weiss, R. The second wave of synthetic biology: from modules to systems. *Nat. Rev. Mol. Cell Biol.* **10**, 410–422 (2009).

81. Weiss, R. & Panke, S. Synthetic biology—paths to moving forward. *Curr. Opin. Biotechnol.* **20**, 447–448 (2009).

82. Slusarczyk, A. L., Lin, A. & Weiss, R. Foundations for the design and implementation of synthetic genetic circuits. *Nat. Rev. Genet.* **13**, 406–420 (2012).

83. Voigt, C. A. Synthetic Biology. *ACS Synth. Biol.* **1**, 1–2 (2012).

84. Stanton, B. C. *et al.* Systematic Transfer of Prokaryotic Sensors and Circuits to Mammalian Cells. *ACS Synth. Biol.* **3**, 880–891 (2014).

85. Tabor, J. J. *et al.* A synthetic genetic edge detection program. *Cell* **137**, 1272–1281 (2009).

86. Nielsen, A. A. K. *et al.* Genetic circuit design automation. *Science* **352**, aac7341–aac7341 (2016).

87. Church, G. M., Elowitz, M. B., Smolke, C. D., Voigt, C. A. & Weiss, R. Realizing the potential of synthetic biology. *Nat. Rev. Mol. Cell Biol.* **15**, 289–294 (2014).

88. Miskin, M. Z. *et al.* Electronically integrated, mass-manufactured, microscopic robots. *Nature* **584**, 557–561 (2020).

89. Yang, X., Chang, L. & Pérez-Arancibia, N. O. An 88-milligram insect-scale autonomous crawling robot driven by a catalytic artificial muscle. *Sci. Robot.* **5**, eaba0015 (2020).

90. Dillinger, C., Nama, N. & Ahmed, D. Ultrasound-activated ciliary bands for microrobotic systems inspired by starfish. *Nat. Commun.* **12**, 6455 (2021).

91. Han, M. *et al.* Submillimeter-scale multimaterial terrestrial robots. *Sci. Robot.* **7**, eabn0602 (2022).

92. Hu, W., Lum, G. Z., Mastrangeli, M. & Sitti, M. Small-scale soft-bodied robot with multimodal locomotion. *Nature* **554**, 81–85 (2018).

93. Li, A. *et al.* Programmable droplet manipulation by a magnetic-actuated robot. *Sci. Adv.* **6**, eaay5808 (2020).

94. Ze, Q. *et al.* Spinning-enabled wireless amphibious origami millirobot. *Nat. Commun.* **13**, 3118 (2022).

95. Cheney, N., Clune, J. & Lipson, H. Evolved Electrophysiological Soft Robots. in (2014). doi:10.7551/978-0-262-32621-6-ch037.

96. Gomes, J., Urbano, P. & Christensen, A. L. Evolution of Swarm Robotics Systems with Novelty Search. *Swarm Intell.* **7**, 115–144 (2013).

97. Kim, S., Laschi, C. & Trimmer, B. Soft robotics: a bioinspired evolution in robotics. *Trends Biotechnol.* **31**, 287–294 (2013).

98. Kriegman, S. *et al.* Automated shapeshifting for function recovery in damaged robots. in *Robotics: Science and Systems XV* (2019). doi:10.15607/RSS.2019.XV.028.

99. Rieffel, J., Knox, D., Smith, S. & Trimmer, B. Growing and Evolving Soft Robots. *Artif. Life* **20**, 143–162 (2014).

100. Rubenstein, M., Cornejo, A. & Nagpal, R. Programmable self-assembly in a thousand-robot swarm. *Science* **345**, 795–799 (2014).

101. Shah, D. *et al.* Shape Changing Robots: Bioinspiration, Simulation, and Physical Realization. *Adv. Mater.* **33**, 2002882 (2021).

102. Lehman, J. *et al.* The Surprising Creativity of Digital Evolution: A Collection of Anecdotes from the Evolutionary Computation and Artificial Life Research Communities. *Artif. Life* **26**, 274–306 (2020).

103. Baluška, F. & Levin, M. On Having No Head: Cognition throughout Biological Systems. *Front. Psychol.* **7**, (2016).

104. Davies, J. A. & Cachat, E. Synthetic biology meets tissue engineering. *Biochem. Soc. Trans.* **44**, 696–701 (2016).

105. Clawson, W. P. & Levin, M. Endless forms most beautiful 2.0: teleonomy and the bioengineering of chimaeric and synthetic organisms. *Biol. J. Linn. Soc.* blac073 (2022) doi:10.1093/biolinnean/blac073.

106. Kauffman, S. A. *The Origins of Order: Self-Organization and Selection in Evolution*. (Oxford University Press, 1993).

107. Roli, A. & Kauffman, S. A. Emergence of Organisms. *Entropy* **22**, 1163 (2020).

108. Nagode, M. & Fajdiga, M. The REBMIX Algorithm and the Univariate Finite Mixture Estimation. *Commun. Stat. - Theory Methods* **40**, 876–892 (2011).

109. Spurek, P. & Tabor, J. Cross-Entropy Clustering. *Pattern Recognit.* **47**, 3046–3059 (2014).

110. Tabor, J., Spurek, P., Kamieniecki, K., Śmieja, M. & Misztal, K. Introduction to Cross-Entropy Clustering The R Package CEC. Preprint at https://doi.org/10.48550/arXiv.1508.04559 (2015).

111. Hansen, J. N., Rassmann, S., Stüven, B., Jurisch-Yaksi, N. & Wachten, D. CiliaQ: a simple, open-source software for automated quantification of ciliary morphology and fluorescence in 2D, 3D, and 4D images. *Eur. Phys. J. E* **44**, 18 (2021).

112. A Very Fast 2D Concave Hull Algorithm. https://joelgombin.github.io/concaveman/.

113. Hahsler, M., Piekenbrock, M. & Doran, D. dbscan: Fast Density-Based Clustering with R. *J. Stat. Softw.* **91**, 1–30 (2019).

114. Maechler, M., Rousseeuw, P., Struyf, A., Hubert, M. & Hornik, K. cluster: Cluster Analysis Basics and Extensions. (2022).

115. Lafarge, T. & Pateiro-Lopez, B. alphashape3d: Implementation of the 3D Alpha-Shape for the Reconstruction of 3D Sets from a Point Cloud. (2020).

116. aoles/RBioFormats: R interface to Bio-Formats version 0.0.75 from GitHub. https://rdrr.io/github/aoles/RBioFormats/.

117. Rvision - A computer vision library for R. (2022).

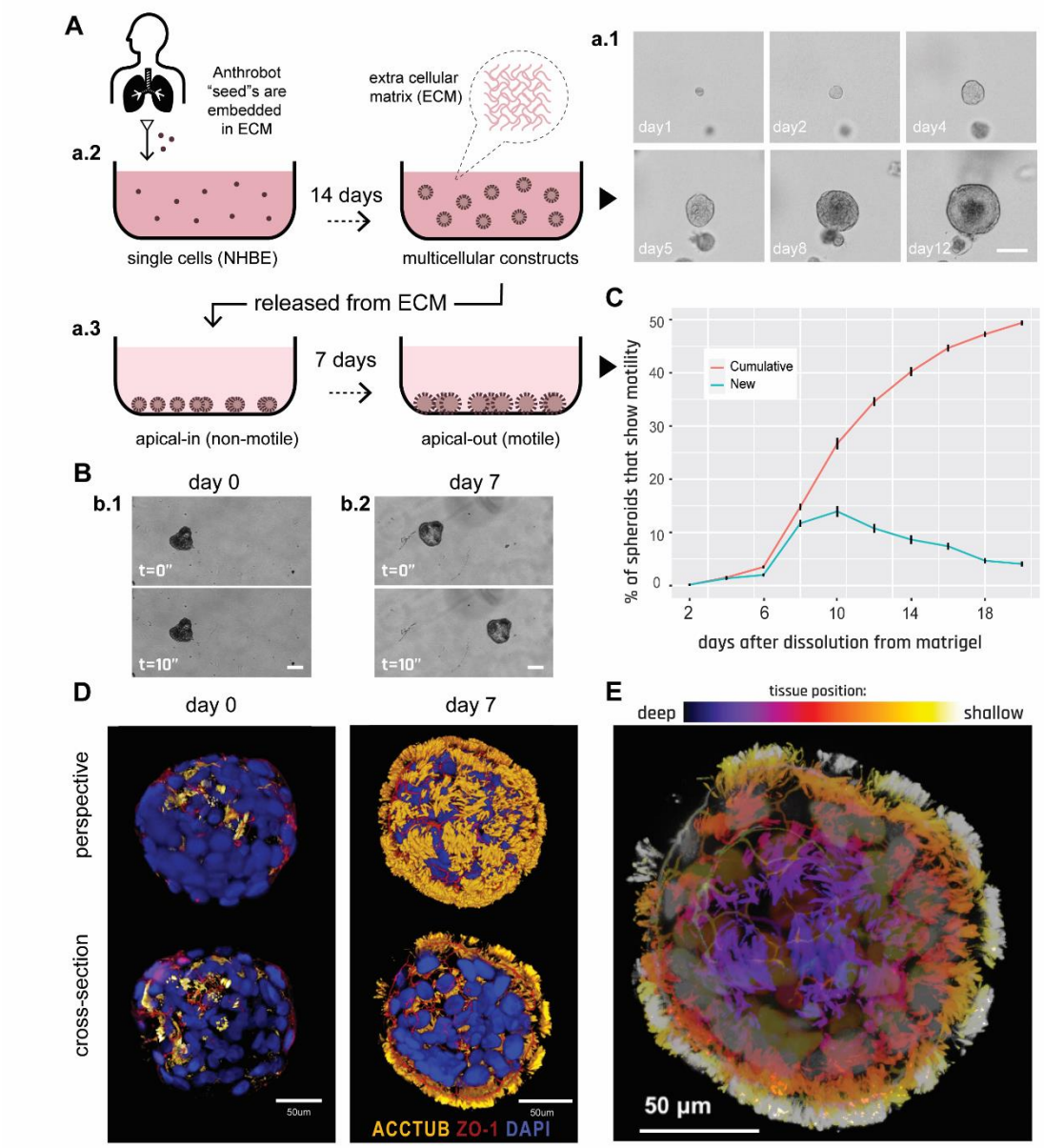

Figure 1 Human bronchial epithelial cells self-construct into multicellular motile living architectures. (A) Workflow for producing Anthrobots. NHBE cells' apical-in to apical-out transition is facilitated by first culturing them in extra cellular matrix (ECM) under appropriate differentiation-inducing conditions), during which time apical-in spheroids self-construct from single cells (a.1), and upon the completion of this 14 day period (a-.2by releasing mature spheroids from the ECM (a.3) and continuing to culture them in low-adhesive environment. Scalebar 50um. (B) Phase contrast images of an apical-in (b.1) and apical-out (b.2) spheroids, captured immediately after dissolution from ECM (day 0) and 7 days after dissolution (day 7), respectively. Day 0 spheroids show no motility, whereas day 7 spheroids show drastically increased motility. Scalebars 50um. (C) Percentage of cumulative and newly motile spheroids in the 22 days following dissolution. Out of the 2281 spheroids characterized total, around 50 % consistently showed no signs of motility (despite having cilia) within this 3-week period and were labeled as non-movers. (D) Immunostaining of day0 and day7 spheroids with a-tubulin (cilia

marker), ZO-1 (tight junction marker), and DAPI (nuclear stain). (E) A mature Anthrobot with depth background. Immunostained with a-tubulin (cilia marker), ZO-1 (tight junction marker), and DAPI (nuclear stain).

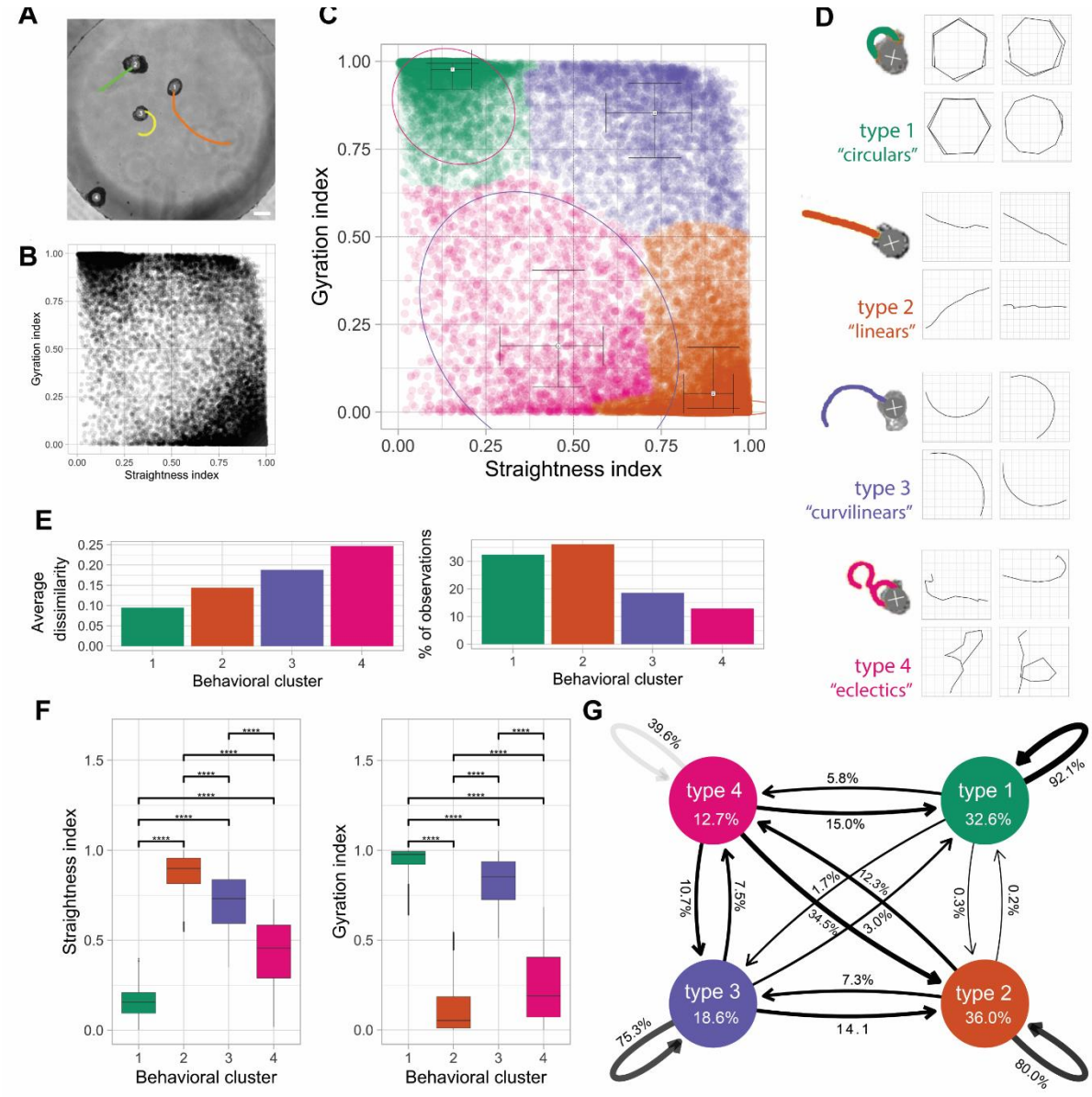

Figure 2. Anthrobots self-organize into discrete movement types. (A) Anthrobots display different movement types. Scalebar 100uM. (B) Distribution of all 30-second periods in the analysis plotted by their straightness and gyration indices, showing signs of clustering near three of the 4 corners of the plot. (C) Clustered scatter plot of all 30-second periods with centers of cluster marked and colored. (D) Prototypical examples from each cluster with 30-second sample trajectories. (E) Quantitative comparison of key characteristics of the four clusters in terms of intra-cluster homogeneity ("average dissimilarity") and occurrence frequency ("% of observations") which show that the largest clusters 1 and 2 have relatively low dissimilarity indicating these are the most consistent behavioral patterns. (F) Comparison of gyration and straightness indices for each cluster with significance levels indicated, showing that each cluster

occupies a unique, quantifiable position in the sample space. (G) Markov chain showing state transitions between different clusters and the degree of commitment to a given behavior (persistence), with eclectics being least persistent. Remarkably, type 1 and 2 bots have the lowest interconversion rate which suggests that they are behaviorally the most orthogonal.

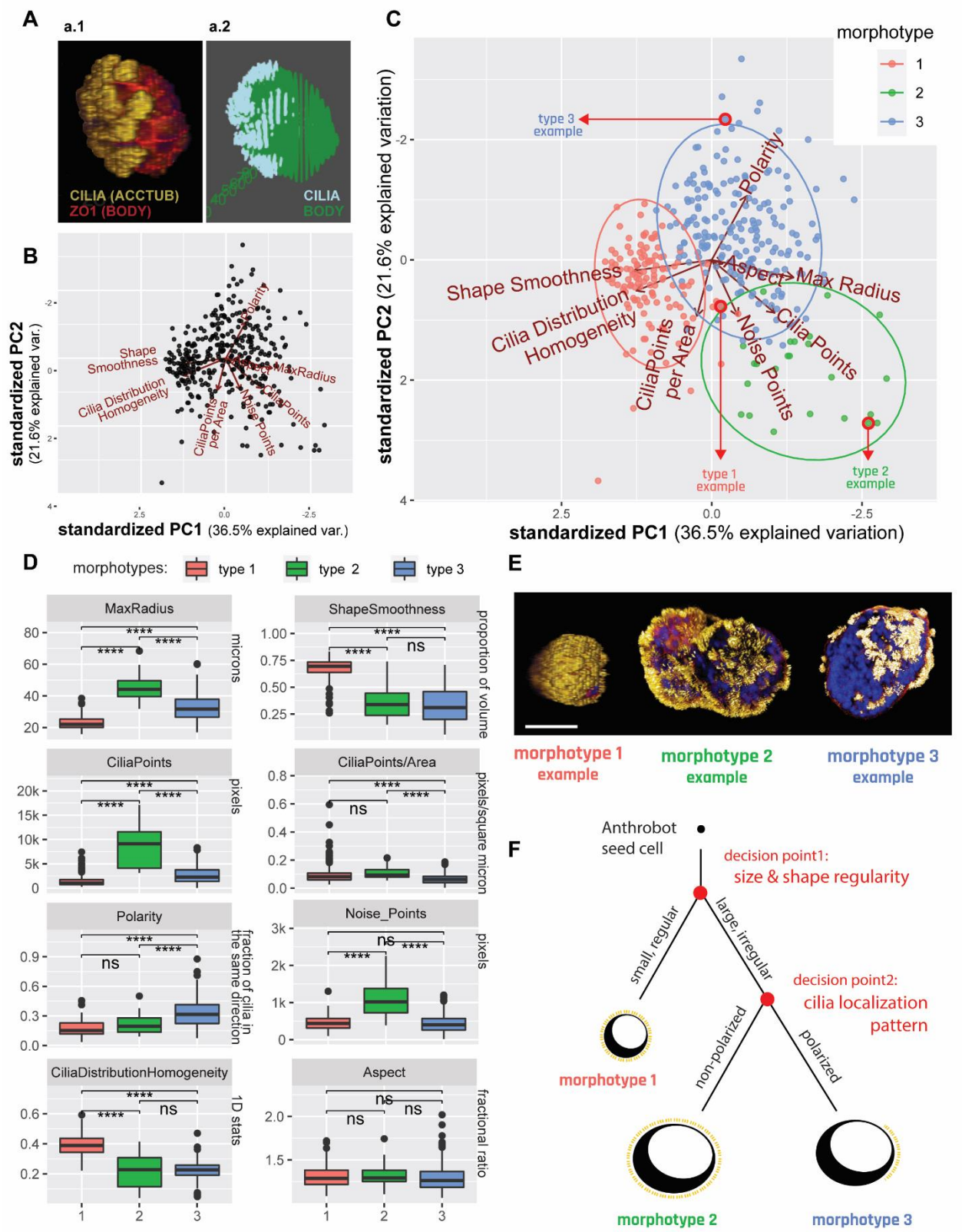

Figure 3. Anthrobots self-organize into distinct morphological types. (A) Anthrobot immunocytochemistry enables morphological classification pipeline. (a1) Sample immunological stain for cilia (acctub, i.e., alpha tubulin) and body mesh formed by the tight junctions (ZO1) (a2) and its binarized

counterpart, showing the Anthrobot body boundaries and cilia localization on the body, represented by a mesh. (B) Binarized body and cilia information from 350 Anthrobots plotted along 8 morphological indices on a PCA cloud. (C) PCA clustered with the unsupervised Ward.D2 method with three morphotypical clusters emerging. Red arrows point to specific examples featured in panel E, selected from the cluster edges for distinct representation. (D) Distinct morphotypes translate with significance to differences in real-life morphological metrics, characterized by 8 variables from which the PCA was computed. (E) Sample morphotype examples for Cluster 1, 2 and 3 chosen for their ability to best represent the cluster. Scalebar 50uM. (F) Decision tree of Anthrobot morphogenesis with two major checkpoints as revealed by the PCA hierarchy: first decision point is size/shape (has equal impact), second decision point is cilia localization pattern.

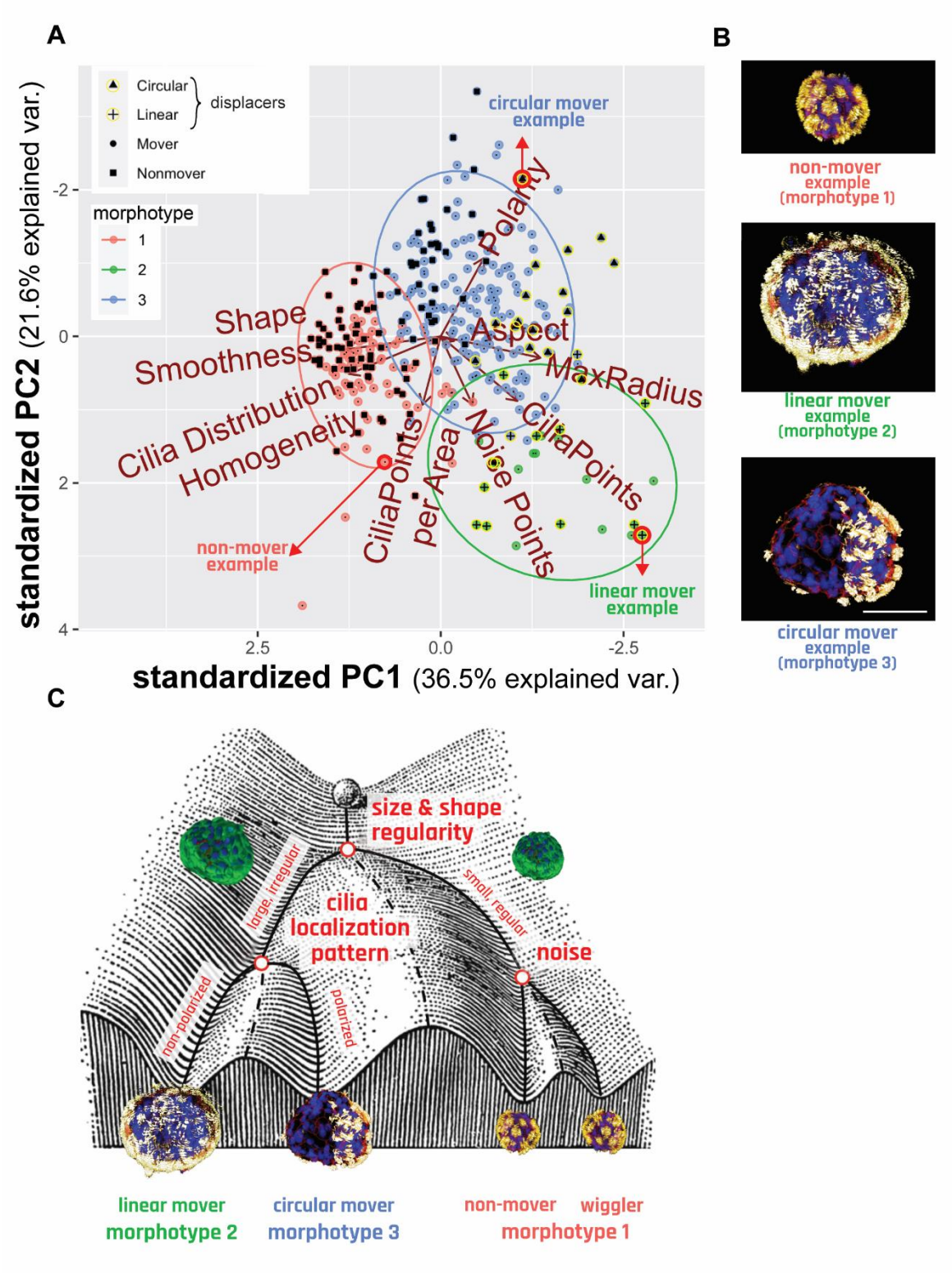

Figure 4. Distinct movement types and morphotypes are highly correlated. (A) PCA of 350 bots forming 3 morphotypical clusters, showing that there is significant overlap between these clusters and the separately marked Non-movers, linears and circulars. Red arrows point to specific examples featured in

panel B, selected from the cluster edges for distinct representation. (B) Sample morphotype examples from each cluster, corresponding to Cluster 1, 2 and 3 and Nonmover, Linear, and Circular, respectively chosen for their ability to best represent the morphotype vs movement type mapping. Scalebar 50uM. (C) Waddington landscape illustrating the logic of determination of bot behavior and their relation to morphotypical indices with end behavioral products, as well as the potential states possible at each level of bifurcation of the bots' development. (Waddington Landscape image modified from J. Ferrell, 2012.)

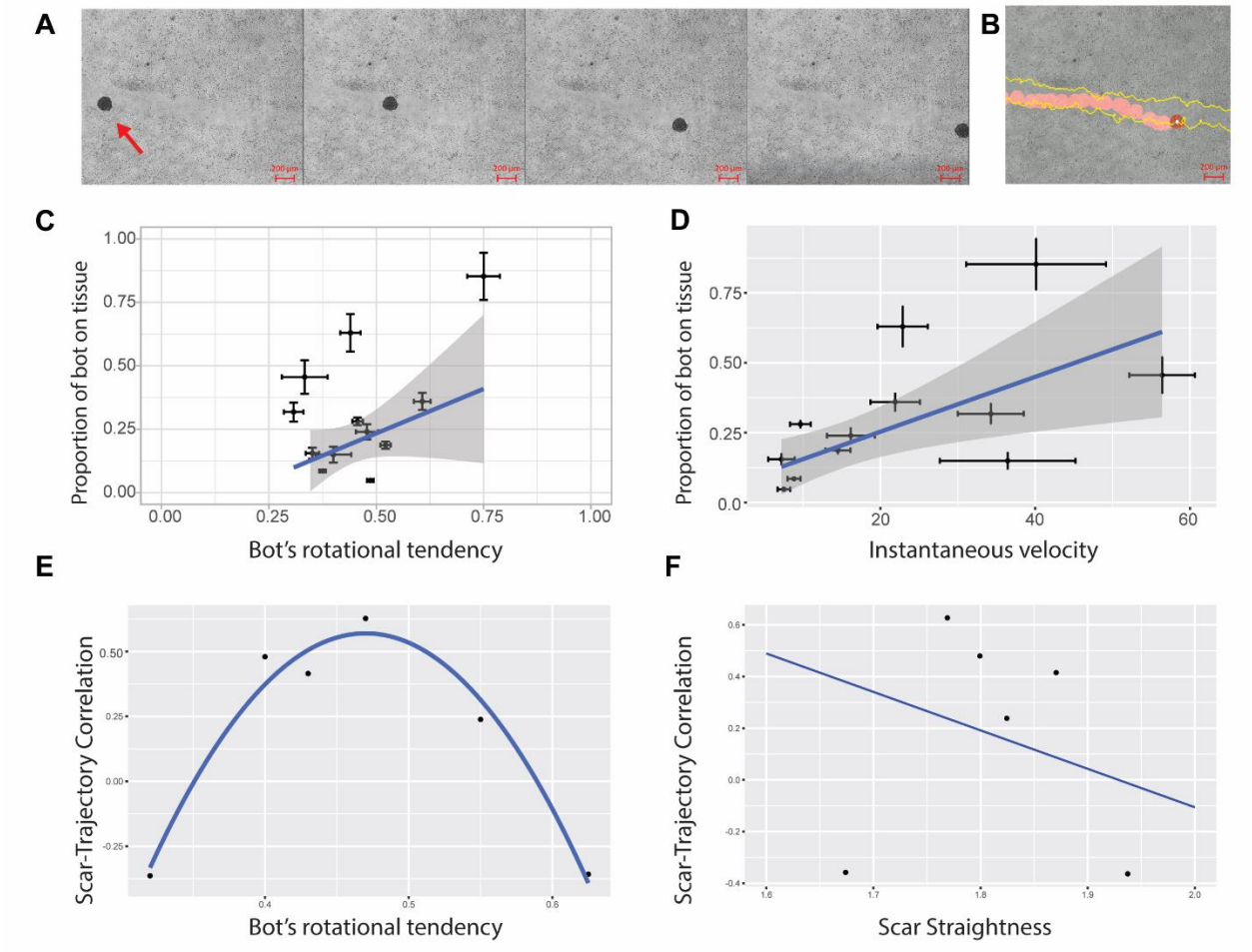

Figure 5. Anthrobots can traverse live tissues. (A) A representative timelapse video of an Anthrobot as it traverses a neural scar in vitro. (B) Sample tracking video output with scar edge highlighted in yellow and bot path in red. The rotation of the bot is measured through the change in the orientation of the green and red bars attached to the center of the bot in white. (C) The significant (p=0.01, slope 1.3) positive relationship between bot gyration index and proportion of bot's body in contact with scar suggest that circular bots explore the edges of the scar more as they traverse the wound. (D) The significant (p=0.04, slope 0.008) positive relationship between bot speed and proportion of bot's body in contact with scar further suggest that faster bots also explore the edges of the scar more as they traverse the wound. (E) For a subset of bots (dataset constrained to non-stalling bots with min 10 microns/second speed), the quadratic relationship (p=0.01) between bot gyration index and scar-trajectory similarity metric suggests that there is a goldilocks zone for how circular bots need to for maximum scar area exploration. (F) For the same subset of bots as in panel E, the significant negative correlation (p=0.04) between scar straightness and scar-trajectory similarity metric further suggest that bots can explore more jagged and more blunt scar interfaces with higher success. $r^2 = 0.99$

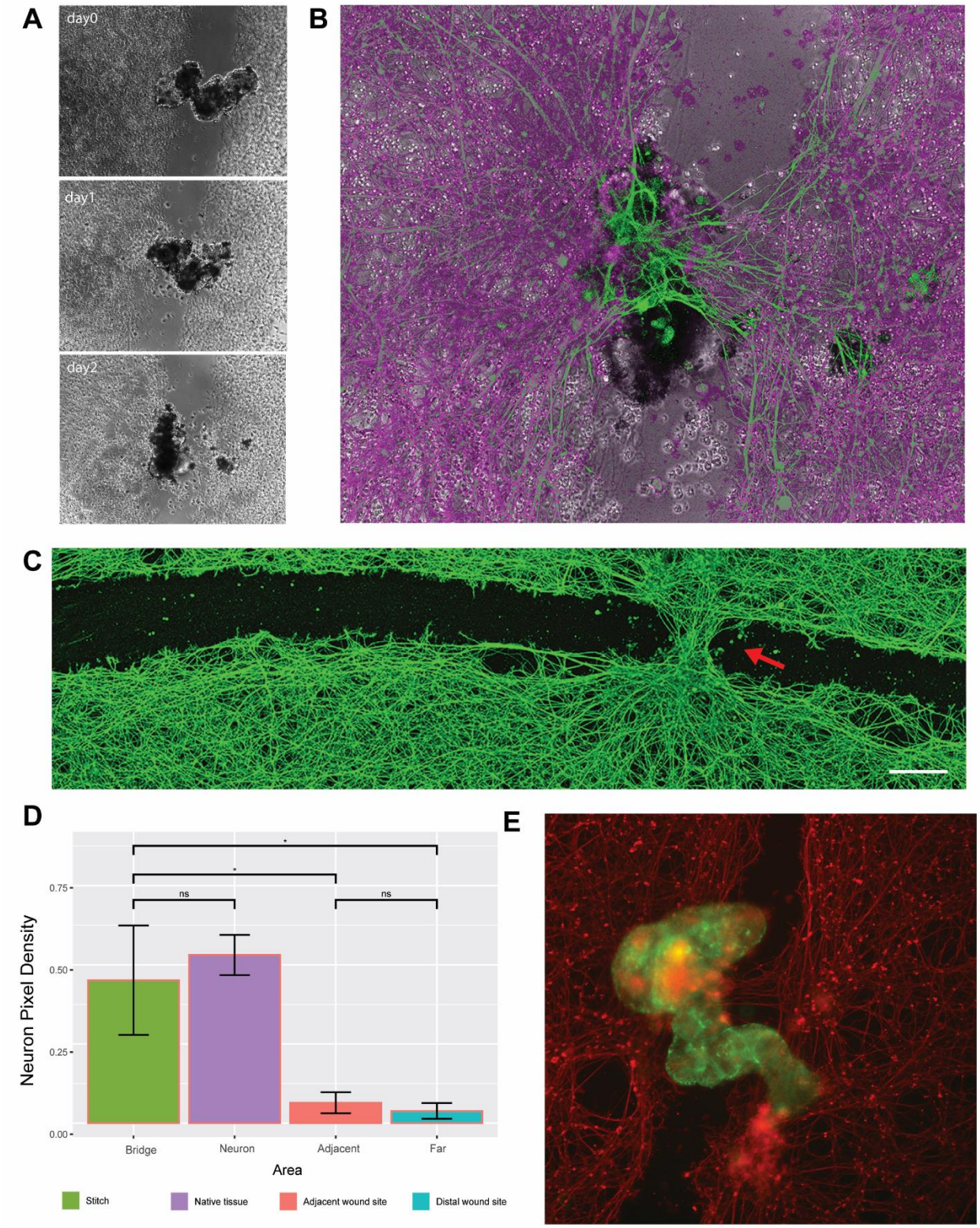

Figure 6. Anthrobots can promote regeneration in live tissue wounds. (A) sample micrograph of a bridge across a neural scar over time. (B) An overlay of a bridge bot and the induced stitch at the end of the

observation. (C) Immunological staining of neurons fixed on day3 after the bots were introduced to the system, showing an induced neural repair at the site of bot settlement. Scalebar 500uM. (D) Average proportion of neuronal coverage by pixel counts for each positional category at the healing (self-stitch) site, unwounded native tissue (calculated by the average of the two neuron heavy area pixel coverage), adjacent areas of scar and further reaches of scar. Difference between stitch site and native tissue is insignificant ($p = 0.37$), while the difference between the stitch site and both adjacent and distal scar sites are significant (w/ $p = 0.006$ and $p = 0.005$, respectively) which suggests the healed tissue is as dense as the native tissue, and the healing effect follow a crisp profile as opposed to a gradient profile. See methods section for example frame of a sampling region. (E) Immunological staining of another sample bridge superbot (green) and the neuronal tissue (red).

Supplemental Figure 1

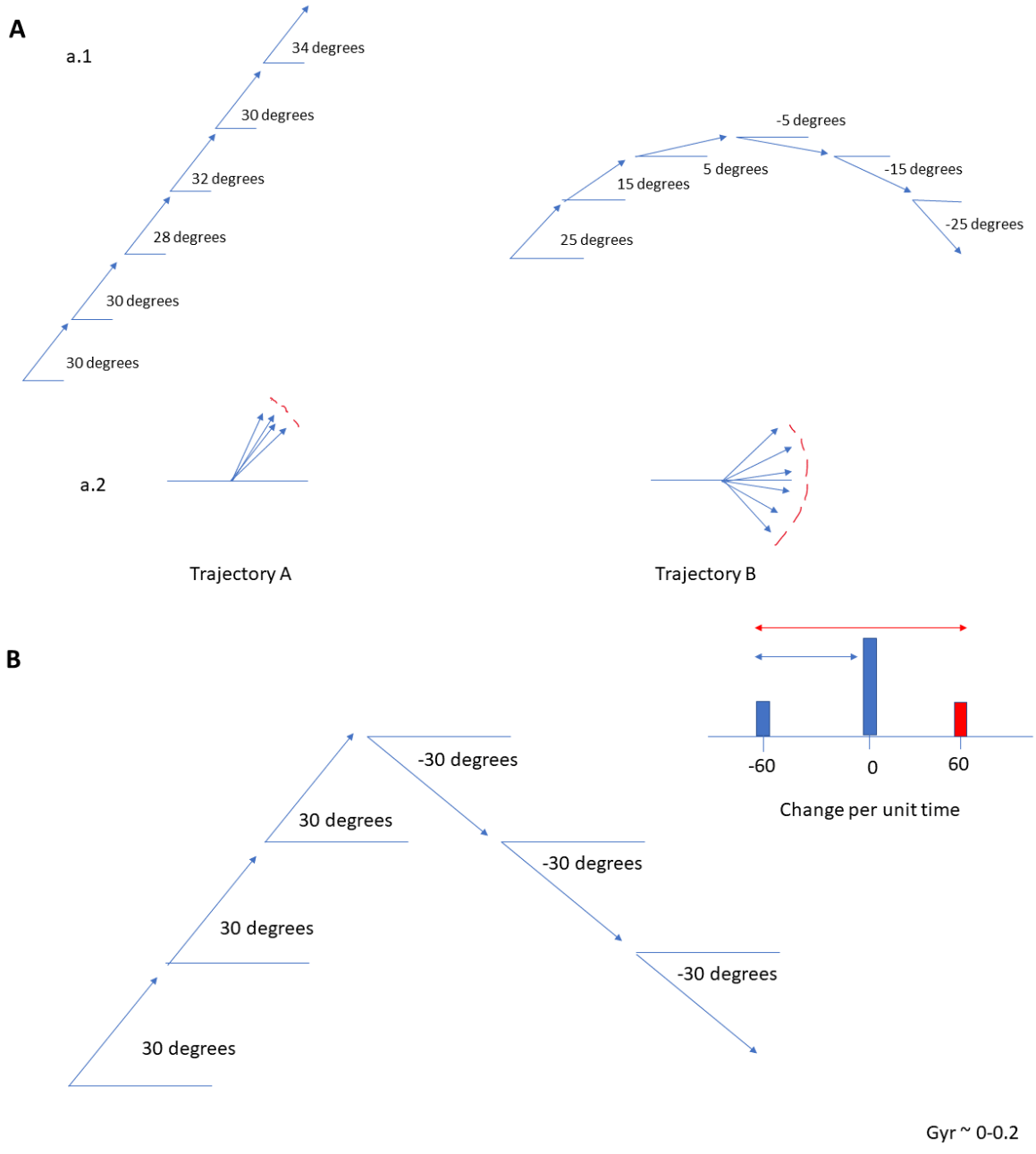

Gyr ~ 0-0.2

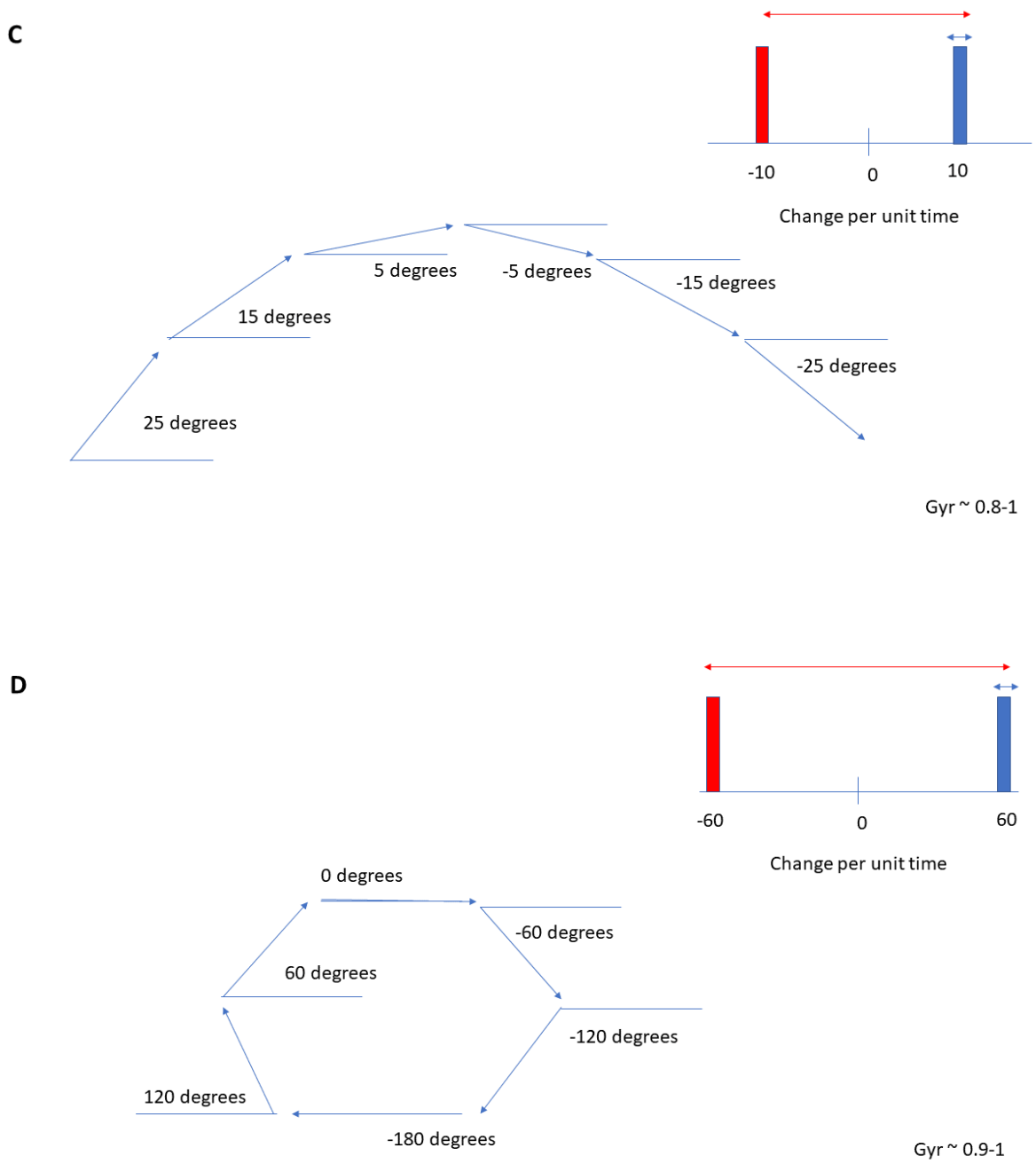

Figure S1 Sample trajectories that reference a relative x-axis to find heading angle. (A) Visual representation of straightness index, which calculates spread of headings as a whole without taking into account temporal dynamics. (B, C, D) Visual representation of gyration index, which includes the temporal aspect and calculates spread of change in headings relative to their magnitude. Graphically, it is represented as the ratio of the blue length (original circular variance) to the red length (circular variance of the original angular speeds and their additive inverse) on the histograms.

Supplemental Figure 2

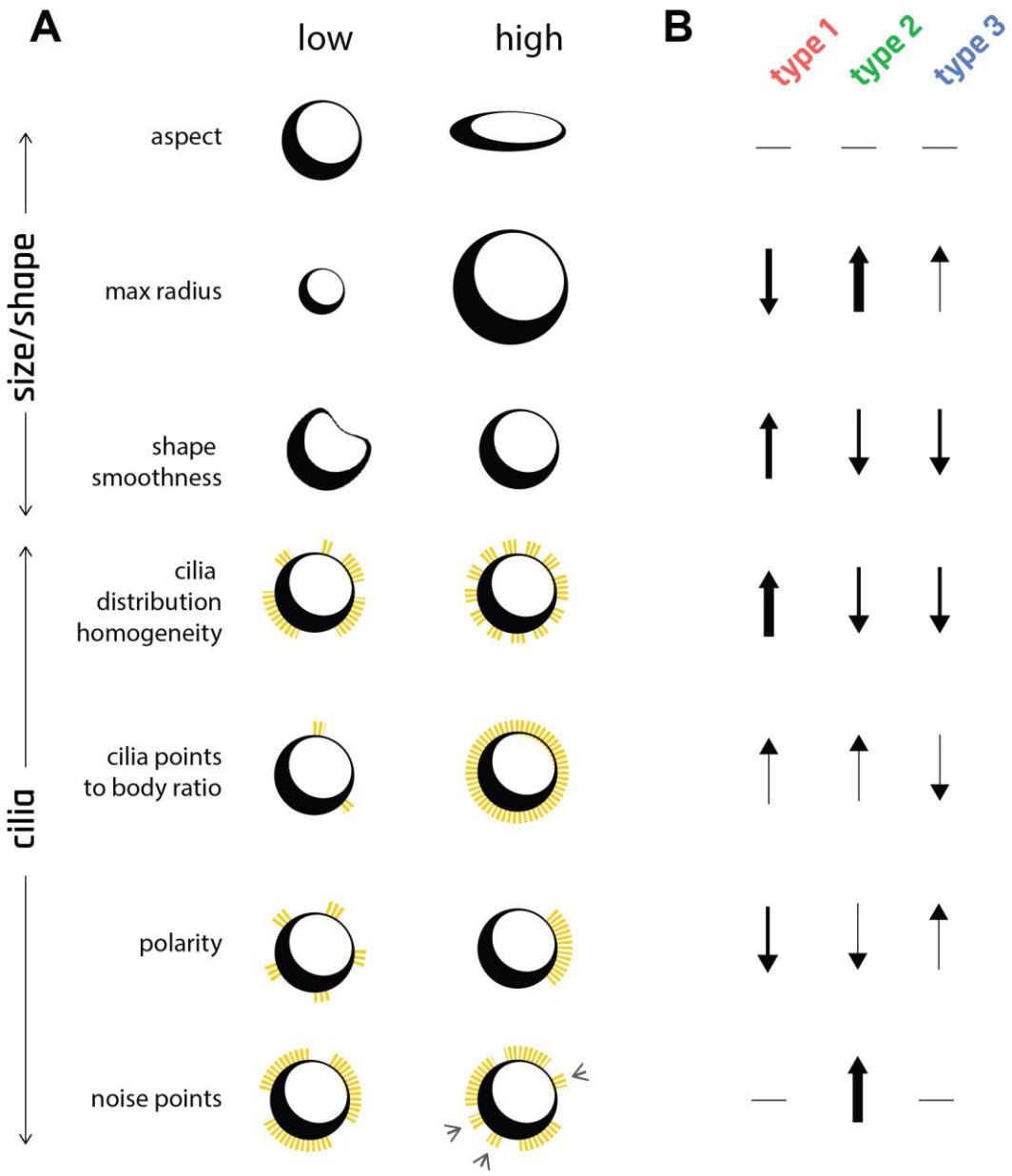

Figure S2. Eight morphological indices were used to characterize Anthrobot morphotypes. (A) Visual summary of morphological indices at their extreme points (low, high). (B) Graphic summary of boxplots on Figure 3D, describing 3 different morphotypes. Arrow thicknesses are correlated with the # of standard deviations between a given morphotype's mean vs the overall population mean for a particular morphological index.

Supplemental Figure 3

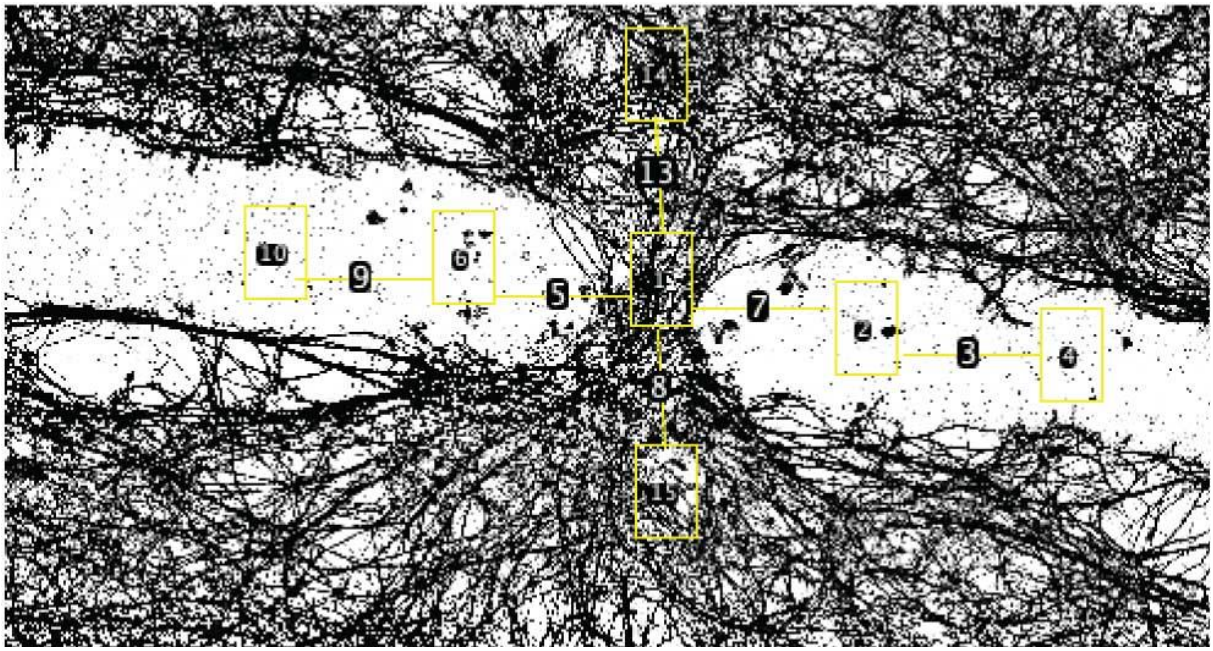

Figure S3 Sample neuronal density sampling region. Each rectangle represents an area sampled and the lines are consistently the same length, the "bridge length".

Supplemental Videos

Please refer to the following directory for the Supplemental Videos:

https://tufts.box.com/s/u5hm3sz4ihh4fr2qw0znq9e2oupcosgg

Video Legends

Supplemental Video 1 - Anthrobots are self-constructing motile biobots, and therefore can be created in a high-throughput manner.

Supplemental Video 2 - Anthrobots exhibit a range of movement patterns. (Higher zoom, narrower arena.)

Supplemental Video 3 - Anthrobots exhibit a range of movement patterns. (Lower zoom, broader arena.)

Supplemental Video 4 - Sample linear mover Anthrobot.

Supplemental Video 5 - Anthrobot with higher circular tendency traverse a neuronal wound.

Supplemental Video 6 - Anthrobot with lower circular tendency traverse a neuronal wound.